

Robust Responses of the Sahelian Hydrological Cycle to Global Warming

SPENCER A. HILL

Department of Atmospheric and Oceanic Sciences, University of California, Los Angeles, and Division of Geological and Planetary Sciences, California Institute of Technology, Pasadena, California

YI MING

NOAA/Geophysical Fluid Dynamics Laboratory, Princeton, New Jersey

MING ZHAO

NOAA/Geophysical Fluid Dynamics Laboratory, Princeton, New Jersey, and University Corporation for Atmospheric Research, Boulder, Colorado

(Manuscript received 18 April 2018, in final form 7 September 2018)

ABSTRACT

How the globally uniform component of sea surface temperature (SST) warming influences rainfall in the African Sahel remains insufficiently studied, despite mean SST warming being among the most robustly simulated and theoretically grounded features of anthropogenic climate change. A prior study using the NOAA Geophysical Fluid Dynamics Laboratory (GFDL) AM2.1 atmospheric general circulation model (AGCM) demonstrated that uniform SST warming strengthens the prevailing northerly advection of dry Saharan air into the Sahel. The present study uses uniform SST warming simulations performed with 7 GFDL and 10 CMIP5 AGCMs to assess the robustness of this drying mechanism across models and uses observations to assess the physical credibility of the severe drying response in AM2.1. In all 17 AGCMs, mean SST warming enhances the free-tropospheric meridional moisture gradient spanning the Sahel and with it the Saharan dry-air advection. Energetically, this is partially balanced by anomalous subsidence, yielding decreased precipitation in 14 of the 17 models. Anomalous subsidence and precipitation are tightly linked across the GFDL models but not the CMIP5 models, precluding the use of this relationship as the start of a causal chain ending in an emergent observational constraint. For AM2.1, cloud-rainfall covariances generate radiative feedbacks on drying through the subsidence mechanism and through surface hydrology that are excessive compared to observations at the interannual time scale. These feedbacks also act in the equilibrium response to uniform warming, calling into question the Sahel's severe drying response to warming in all coupled models using AM2.1.

1. Introduction

The hydrological cycle of the semiarid Sahel reflects a competition between the year-round drying influence of the Sahara Desert to the north and the wetting influence

of moist tropical circulations expanding from the south during boreal summer [comprising the West African monsoon in the western Sahel (e.g., Nicholson 2013) and continental convection in the eastern Sahel (e.g., Nicholson 2018)]. The relative strengths of these drying and moistening influences have varied on interannual (e.g., Pomposi et al. 2016), decadal (e.g., Biasutti and Giannini 2006), and millennial (e.g., Tierney et al. 2017) time scales, as indicated by corresponding variations in precipitation and other hydrological variables. Anthropogenic global warming is also likely to alter this balance, but general circulation model (GCM) projections of future Sahelian hydrological cycle change are uncertain even in sign, with little decrease in spread across

 Denotes content that is immediately available upon publication as open access.

 Supplemental information related to this paper is available at the Journals Online website: <https://doi.org/10.1175/JCLI-D-18-0238.s1>.

Corresponding author: Spencer Hill, shill@atmos.ucla.edu

DOI: 10.1175/JCLI-D-18-0238.1

© 2018 American Meteorological Society. For information regarding reuse of this content and general copyright information, consult the [AMS Copyright Policy](https://www.ametsoc.org/PUBSReuseLicenses) (www.ametsoc.org/PUBSReuseLicenses).

the past two model generations [see review by Rodríguez-Fonseca et al. (2015)].

For at least one atmospheric GCM (AGCM)—NOAA Geophysical Fluid Dynamics Laboratory AM2.1—the global mean (i.e., uniform) component of SST warming induces severe drying in the Sahel that dominates its rainfall change in coupled simulations under future anthropogenic forcing (Held et al. 2005; Lu and Delworth 2005). Hill et al. (2017, hereafter H17) use the column-integrated moist static energy (MSE) budget to show that this is driven by an enhancement of the prevailing MSE and moisture differences between the Sahel and the Sahara acted upon by prevailing northerly winds in the free troposphere: the resulting anomalous advection of dry, low-MSE air into the Sahel inhibits moist convection. This “upped-ante”-like mechanism of drying along a convection zone margin under global warming (Chou and Neelin 2004) relies solely on climatological northerly free-tropospheric flow, the climatological meridional moisture gradient, and an enhancement of that gradient under global warming—the latter being a robust feature of warming simulations (Mitchell et al. 1987; Held and Soden 2006).

It thus seems plausible that this mechanism operates robustly across models and in the real world as global mean temperature increases. Indeed, Gaetani et al. (2017) document reduced wet-season precipitation in the Sahel in all AGCMs from phase 5 of the Coupled Model Intercomparison Project (CMIP5; Taylor et al. 2012) subjected to uniform 4-K SST warming. However, H17 also show that the magnitude of the anomalous dry advection and its attendant impact on precipitation are sensitive to how moist convection is parameterized—Sahelian precipitation in AM2.1 *increases* slightly under uniform SST warming if an alternate convective parameterization is used. Given the diversity of formulations of convective physics (and all other processes) across AGCMs and their crudity compared to the real world, it thus also seems plausible that this mechanism is, in fact, not robust.

H17 also speculate that the Sahelian rainfall response to SST warming depends on the climatological depth of convection locally as follows: 1) the height to which the additional near-surface heat and water vapor generated by SST warming gets transported should increase with the depth of the prevailing convection locally; 2) the meridional MSE gradient spanning the Sahel and Sahara will therefore be enhanced over a greater depth of the troposphere if the climatological ascent profile in the Sahel is more “top-heavy”; 3) this causes the anomalous column-integrated northerly low-MSE advection to be greater; and 4) this is balanced by greater anomalous subsidence, ultimately yielding 5) greater reductions in

precipitation. Globally, Chen et al. (2016) demonstrate similar behavior in their analysis of climatological convecting regions in which precipitation increases under future warming simulations): ascent is typically enhanced where the climatological ascent profile is top-heavy (i.e., deep) and typically suppressed where it is “bottom-heavy” (i.e., shallow).

If verified, such a correlation between the drying response and the present-day circulation could lead to an “emergent constraint”—that is, an observed real-world field that can falsify model responses whose corresponding fields in present-day simulations are sufficiently removed from the observational value. Among other factors, this requires a sufficiently quantitatively accurate relationship between the fields involved at each intermediate step of the proposed causal chain [see review by Klein and Hall (2015)]. For the H17 mechanism, the first step is the link between anomalous subsidence and anomalous precipitation.

Central to the severity of the Sahelian drying response to warming in AM2.1 is the Sahel’s weak top-of-atmosphere (TOA) radiative response (H17): given enhanced northerly low-MSE advection, less anomalous subsidence would be required if the net column energetic forcing (for land regions, equivalent to the TOA radiative flux) also decreased.¹ No theory has been posited for this TOA radiative response, and simulations in AM2.1 with a wide range of imposed uniform SST perturbations suggest that it is sensitive to the imposed SST warming magnitude (H17). Cloud radiative changes can also influence precipitation in semiarid regions through their influence on surface radiative fluxes, for example if cloud loss yields increased radiative fluxes onto a desiccated surface, thereby driving surface warming and reduced boundary layer relative humidity. It is therefore important to assess the TOA and surface radiative response in other models and, to the extent possible, in observations. The latter is possible using observations of interannual

¹This can be seen from the perturbation MSE budget diagnosed for AM2.1 by H17: $\{(\delta\bar{w})(\partial\bar{h}/\partial p)\} + \{\bar{u} \cdot \nabla(\delta\bar{h})\} \approx \delta\bar{F}_{\text{net}}$, where h is MSE, overbars denote monthly averages, curly brackets denote column integrals, δ denotes the equilibrium difference between the +2-K and control simulations averaged over July–September, and all other notation is standard. Omitted in this expression are the anomalous energy storage and transient eddy MSE flux divergence terms, which were comparatively weak (see their Table 2). The anomalous net energetic forcing $\delta\bar{F}_{\text{net}}$ was also weak, leading to a leading-order balance between the anomalous advection terms, requiring descent ($\delta\bar{w} > 0$) in the mid- to upper troposphere, where $\partial_p\bar{h} < 0$. Supposing that instead $\delta\bar{F}_{\text{net}} < 0$ and for the same horizontal advection anomaly, then $\delta\bar{w}$ will be smaller, presumably resulting in a weaker precipitation reduction. See Eq. (3) of H17 and corresponding text for further details.

TABLE 1. GFDL atmospheric models used in this study. Columns, from left to right, indicate model name, publication documenting the model, observational SST dataset and year range used to create the climatological annual cycle of SSTs, and length of simulation.

Model	Reference	SST data	Duration (yr)
AM2.1	Anderson et al. (2004)	Reynolds et al. (2002), 1981–99	30
AM2.1-UW	Hill et al. (2017)	Reynolds et al. (2002), 1981–99	30
AM2.5	Delworth et al. (2012)	Reynolds et al. (2002), 1981–99	20
AM3	Donner et al. (2011)	Hurrell et al. (2008), 1981–2000	30
c90-AM3	None	Hurrell et al. (2008), 1981–2000	10
c180-HiRAM	Zhao et al. (2009)	Rayner et al. (2003), 1981–2005	17
c48-HiRAM	Zhao (2014)	Rayner et al. (2003), 1981–2005	15

covariances of Sahelian precipitation and radiative fluxes, provided that the interannual variations and the equilibrium response to warming can be demonstrated to involve the same mechanisms.

Here, we address these issues by extending the analyses of H17 to 6 other GFDL model variants and 10 CMIP5 models and comparing them to observational data. After detailing our methodology (section 2), we present the hydrological (section 3) and MSE budget (section 4) results of uniform SST warming simulations in the GFDL and CMIP5 models. All 17 models examined exhibit the H17 mechanism to some degree, including an enhanced meridional MSE gradient, increased northerly dry advection, and anomalous subsidence over an appreciable depth of the free troposphere. These lead to reduced precipitation in the Sahel in all models except three from GFDL that share a particular convective parameterization. Of the 14 drying models, AM2.1 is the only one in which the net energetic forcing of the Sahel does not decrease appreciably with warming.

We then demonstrate that, despite this mechanism’s qualitative robustness, the link between anomalous precipitation and anomalous subsidence is not sufficiently accurate across the CMIP5 models to form the basis for an emergent observational constraint (section 5). Finally, we show that the Sahel’s TOA and surface radiative flux responses to warming in AM2.1 that positively feed back on drying depend on cloud radiative changes that also emerge on the interannual time scale and are excessive compared to observations (section 6). We conclude with a discussion (section 7) and summary (section 8).

2. Methodology

a. GFDL models and simulations

We examine present-day control and uniform 2-K SST warming simulations in the seven GFDL model variants listed in Table 1. AM2.1 is as described in H17; briefly, it features a finite-volume, ~ 200 -km resolution, latitude–longitude dynamical core, 24 vertical levels

extending to 10 hPa, the relaxed Arakawa–Schubert (RAS) convection scheme (Arakawa and Schubert 1974; Moorthi and Suarez 1992), prescribed monthly aerosol burdens, and the LM2 land model (Milly and Shmakin 2002). Both the standard AM2.1 and the variant from H17 that replaces RAS with the University of Washington convective parameterization (UW; Bretherton et al. 2004) are included in this study; they are hereafter referred to respectively as AM2.1 and AM2.1-UW. AM3 (Donner et al. 2011) features a finite-volume, ~ 200 -km cubed-sphere dynamical core, 48 vertical levels extending to 1 hPa, the Donner deep (Donner 1993; Donner et al. 2001) and UW shallow convective parameterizations, comprehensive atmospheric chemistry, online interactive aerosols, a cloud microphysical parameterization that depends on aerosol burdens for stratiform clouds (Ming et al. 2006, 2007), and the LM3 land model (Donner et al. 2011; Milly et al. 2014). The c180-HiRAM model (Zhao et al. 2009) features the same dynamical core as AM3 but with ~ 50 -km horizontal resolution, 32 vertical levels extending to 10 hPa, the UW convection scheme for both deep and shallow convection (although with much convection handled at the grid scale), a relatively simple diagnostic cloud fraction scheme, the LM3 land model, and all other settings taken from AM2.1. Essentially, AM3 was developed from AM2.1 by increasing physical complexity but not resolution, and c180-HiRAM was developed from AM2.1 by increasing resolution but not physical complexity.

The remaining three GFDL AGCMs are alternate-resolution versions of AM2.1, AM3, and c180-HiRAM. AM2.5 (Delworth et al. 2012) is a ~ 50 -km resolution, modestly retuned version of AM2.1, but using the cubed-sphere dynamical core, 32 vertical levels, and the LM3 land model. The c90-AM3 is identical to AM3 other than roughly doubled horizontal resolution; the “c90” notation signifies that each of the six faces of the cubed-sphere grid houses 90×90 grid cells. The standard AM3 resolution is c48. Finally, c48-HiRAM (Zhao 2014) is a ~ 200 -km resolution version of c180-HiRAM (whose resolution is c180), with a reduction in

the land–ocean entrainment parameter ratio as described in Zhao et al. (2009) and in H17 for AM2.1-UW.

Each model has a pair of standard control and +2-K simulations, although among models there are differences in their duration, the underlying SST dataset, and the years averaged over to generate the climatological annual cycle of SSTs repeated each year (Table 1).² We have tested the sensitivity to these differences by repeating the control and +2-K simulations in AM2.1 with each SST field used by other models. The Sahel precipitation responses are similar in each case (not shown), and we assume this holds for the other models.

b. CMIP5 models and simulations

We examine the “amip” and “amip4K” CMIP5 experiments in 10 AGCMs for which the necessary data are available, listed in Table 2.³ These simulations use a time series of observed SSTs from the Hurrell et al. (2008) dataset spanning 1979–2008. Atmospheric composition is also time varying, with the same inputs as in the coupled “historical” CMIP5 simulation. In the +4K simulation, 4K is added uniformly to this time series of SSTs. Averages are taken over the full 30-yr period.

Because the imposed SST warming differs between the GFDL and CMIP5 ensembles, we present all responses normalized by the imposed SST warming. However, as we will discuss below, there is evidence that the two ensembles of models behave distinctly from each other even with this normalization.

c. Interpolation, region definition, and hydrological fields used

All fields are computed on the native horizontal grid of the model’s output and then regridded to a common $1^\circ \times 1^\circ$ grid via bilinear interpolation before plotting or regionally averaging. As in H17, we analyze the Sahel wet season of July–September (JAS) and use a conventional definition of the Sahel as land points spanning 10° – 20° N, 18° W– 40° E.

Although we focus on precipitation, Scheff et al. (2017) demonstrate that there is no single catch-all notion

TABLE 2. Names and modeling institutions of the CMIP5 AGCMs used in this study. CMIP5 model information and outputs are available through the Earth System Grid Federation archive (<http://cmip-pcmdi.llnl.gov/cmip5>).

Model	Institution
BCC-CSM1	Beijing Climate Center
CNRM-CM5	Centre National de Recherches Météorologiques
FGOALS-g2	Institute of Atmospheric Physics, Chinese Academy of Sciences
IPSL-CM5A-LR	Institut Pierre-Simon Laplace
IPSL-CM5B-LR	Institut Pierre-Simon Laplace
MIROC5	Agency for Marine-Earth Science and Technology
MPI-ESM-LR	Max Planck Institute for Meteorology
MPI-ESM-MR	Max Planck Institute for Meteorology
MRI-CGCM3	Meteorological Research Institute
NCAR-CCSM4	National Corporation for Atmospheric Research

of “drying” or “wetting” that fully characterizes a region’s hydrological or vegetative response to global temperature change. As such, we also present convective precipitation, large-scale precipitation, evapotranspiration, precipitation minus evapotranspiration, relative humidity at 925 hPa, and potential evapotranspiration, the latter computed as 80% of the net radiative flux directed into the surface (Milly and Dunne 2016).

d. MSE budget computations

We use monthly, pressure-interpolated data for all vertically defined quantities. The lack of high-frequency data available for the CMIP5 simulations and some of the GFDL simulations prevents the use of the adjustment method of H17 (see their appendixes A and B) to ensure budget closure. The large budget residuals (Seager and Henderson 2013) when using unadjusted data preclude meaningful quantitative analysis of individual budget terms as in H17. For this reason, we do not present column-integrated budget quantities apart from the directly outputted top-of-atmosphere (TOA) radiative fluxes. Instead, we present vertical profiles of the horizontal and vertical MSE advection and their components. Comparison in AM2.1 of the vertical profiles computed using the adjusted high-frequency data on model-native coordinates and the solid ice component as in H17 versus the more approximate method here indicate qualitative insensitivity to these differences throughout the free troposphere (not shown).

In the GFDL models, we use non-frozen MSE, $h \equiv c_p T + gz + L_v q$ in the calculations of moist static stability and vertical MSE advection, where all notation is standard. For the CMIP5 models, the available data comprise time series of pressure-interpolated monthly

² In c180-HiRAM, the applied SST perturbation was inadvertently +2.04 K rather than exactly +2 K. In AM3, aerosol emissions (rather than burdens) are prescribed at near-present-day climatological values, due to that model’s online treatment of aerosols.

³ Two of these, BCC-CSM1 and NCAR-CCSM4, are among the CMIP5 models identified by Zhou et al. (2015) as exhibiting an erroneous zonal oscillation in the TOA downwelling shortwave radiation. This does not affect the Sahel rainfall climatologies or responses in any immediately identifiable way.

averages and in most cases lack geopotential height and the specific mass of ice water. As such, we compute the MSE horizontal gradients using the sum of the sensible and latent heat terms [i.e., for the meridional direction $\partial_y h \approx \partial_y (c_p T + L_v q)$, where ∂_y is a meridional derivative]. Comparison of the Sahel region-mean gradient computed with and without the geopotential term in the GFDL control models confirms that this is reasonably accurate (not shown). Conversely, for vertical MSE advection, we attempted to compute geopotential height using the hypsometric equation: $gz = R_d \int_p^{p_{\text{stc}}} T_v d \ln p$, where T_v is virtual temperature and all other notation is standard. Although differences in the GFDL models between MSE using the model-outputted height and this calculation are small (generally a few percent or less), they lead to large errors in the vertical advection calculations (not shown). Therefore, we do not present moist static stability or vertical MSE advection for the CMIP5 models.

e. Observational data

We analyze TOA radiative fluxes from the CERES-EBAF v4.0 satellite-based observational dataset (Loeb et al. 2018), which spans 2000–17. These include the all-sky net radiative flux, the clear-sky net radiative flux, and the net, shortwave, and longwave cloud radiative effect (i.e., the difference between the all-sky and clear-sky values), all signed positive into the atmosphere. For precipitation and surface temperature, we use the Climate Research Unit (CRU) TS v4.01 dataset (Harris et al. 2014). Climatologies are computed as averages over 1980–2005, chosen to overlap as well as possible with the various periods used for the SSTs (cf. Table 1). All observational values are reinterpolated to the same grid as the models before regional averages are performed.

f. “Extended AMIP” simulations

We examine so-called extended AMIP simulations in AM2.1 and AM3 respectively spanning 1870–99 and 1870–2005. As in the CMIP5 amip specification, the atmospheric composition (or emissions for AM3) vary in time according to historical estimates, as do the SSTs and sea ice. We also compare to a standard CMIP5-protocol 1979–2009 amip simulation in c180-HiRAM [note that the SST dataset used is HadISST rather than Hurrell et al. (2008); cf. Flannaghan et al. 2014]. Results are reinterpolated to the same $1^\circ \times 1^\circ$ grid described above. Multiple ensemble members are available for each of these simulations (10, 3, and 2 in AM2.1, AM3, and HiRAM, respectively); we present results from the first member of each ensemble, but results are qualitatively

insensitive to the choice of member or if the ensemble average is used (not shown).

3. Hydrological responses to uniform SST warming

Figure 1 shows precipitation in the control simulations and its response to 2-K SST warming in the GFDL models, and Table 3 lists the corresponding Sahel region-mean values. Figure 2 and Table 4 show the same for the CMIP5 simulations. Figure 1 also shows the CRU observational estimate of the JAS climatological precipitation. The control precipitation distributions are broadly similar across the models, featuring precipitation decreasing over the continent moving northward into the Sahel as in the observations, with AM2.1-UW exhibiting the most zonal heterogeneity. The control simulation region-mean precipitation varies over a narrower range across the GFDL models than across the CMIP5 models (2.5–4.6 and 1.3–5.5 mm day⁻¹, respectively), and the GFDL ensemble is, on average, wetter than the CMIP5 ensemble (multimodel means of 3.4 and 2.8 mm day⁻¹, respectively). These ensemble means bracket the CRU observational estimate of 3.0 mm day⁻¹.

In the three GFDL models that use the UW convection scheme (c180-HiRAM, c48-HiRAM, and AM2.1-UW), Sahel region-mean precipitation either responds weakly (c180-HiRAM) or increases—fairly uniformly over the southern Sahel in AM2.1-UW, and primarily in the central Sahel where climatological precipitation values are large in c48-HiRAM.⁴ But in all 14 other models, precipitation decreases, from -0.08 mm day⁻¹ K⁻¹ in IPSL-CM5A-LR to -0.67 mm day⁻¹ K⁻¹ in AM2.1. Precipitation reductions generally span the whole width of the Sahel and are larger in the south where rainfall is also climatologically greater (NCAR-CCSM4 is an exception). In contrast to the drying over much of West Africa in most models, precipitation increases over some portion of the Atlantic ITCZ in all 17 models, highlighting that the continental convection is not merely an extension onto land of the adjacent oceanic ITCZ (although this apparent shift of moist convection from land to ocean is likely partly an artifact of warming SSTs without changing the radiative forcing agents; e.g., He and Soden 2017).

In each higher-resolution GFDL model variant, control simulation rainfall in the Sahel is greater than the lower-resolution counterpart, but there is no clear

⁴ All nine members of the c48-HiRAM perturbed physics ensemble of Zhao (2014) are drier in the control (2.4 to 3.3 mm day⁻¹) and wetten the region more (+5 to +22%) than c180-HiRAM (not shown).

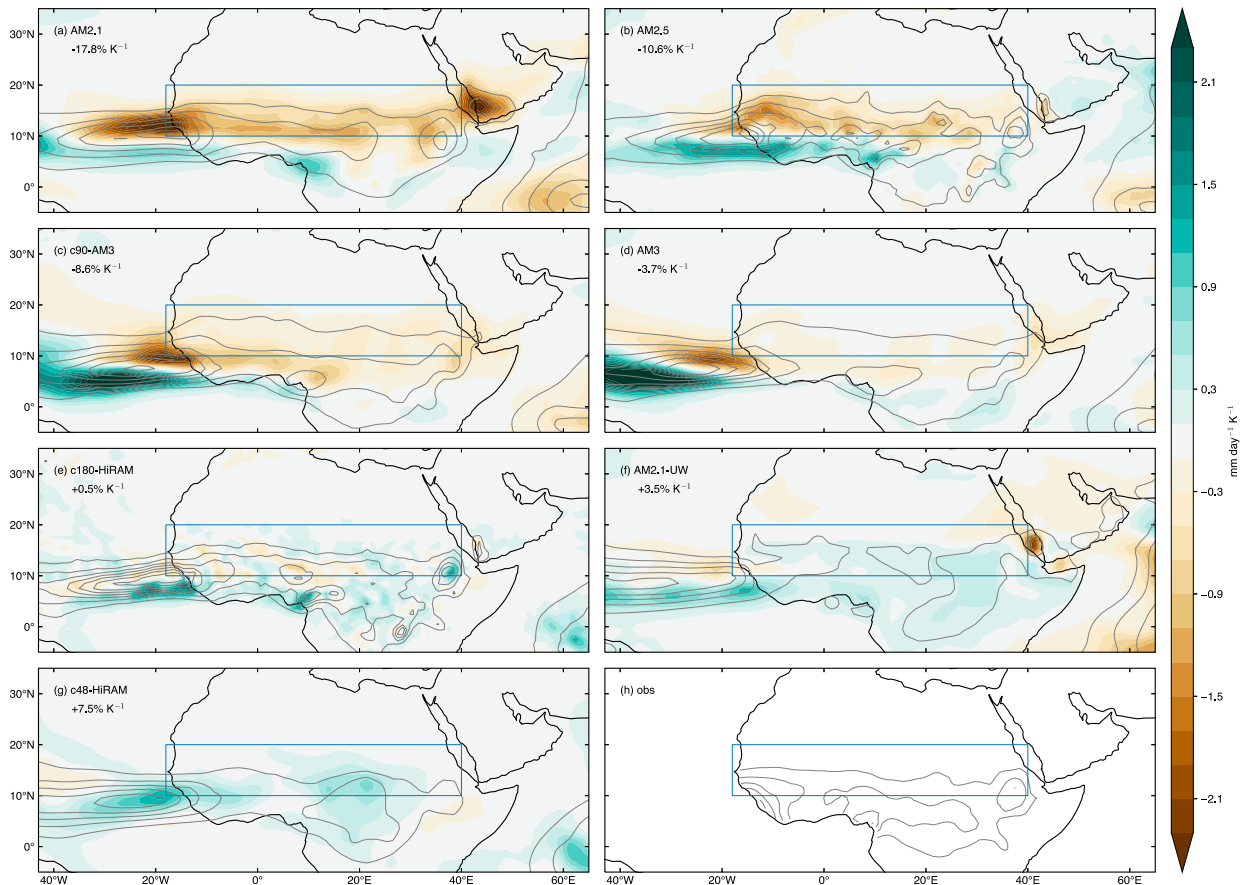


FIG. 1. (a)–(g) Shaded contours indicate the difference in precipitation per unit of SST warming between simulation with uniform 2-K SST warming and present-day control simulation ($\text{mm day}^{-1} \text{K}^{-1}$) and gray contours indicate precipitation in the control simulation, with contours starting at 3 mm day^{-1} and with a 3 mm day^{-1} interval, in each of the 7 GFDL models. The models are ordered from (a) to (g) based on their precipitation response from most negative to most positive within the GFDL ensemble (see Table 3). Values below the model name are that model's Sahel region-mean fractional precipitation change per unit of SST warming. (h) The 1980–2005 climatological JAS precipitation over land in the CRU TS v4.01 dataset, with the same contouring interval as (a)–(g).

relationship between model resolution and the precipitation response to SST warming (Table 3) or between the control simulation precipitation and the response.⁵

⁵ Printed in each panel of Figs. 1 and 2 is that model's Sahel region-mean fractional change in precipitation (i.e., the precipitation change divided by the control simulation value). Whereas the ranking of the GFDL models is identical whether fractional or absolute responses are used, there is no correspondence between the fractional and absolute changes in the CMIP5 models. Even for the GFDL models, the precipitation response does not scale with the climatological value—c180-HiRAM has the second largest control precipitation value (3.9 mm day^{-1}) of the GFDL models, but this does not affect its ranking in terms of fractional changes because the absolute change is simply very small ($+0.02 \text{ mm day}^{-1} \text{K}^{-1}$).

Tables 3 and 4 also list control and perturbation values of all other surface hydroclimatic fields analyzed. In the UW convection models, the nonnegative total precipitation response is driven by increased convective precipitation; the large-scale precipitation, as in all other models, decreases. Evapotranspiration also increases, in AM2.1-UW and c180-HiRAM at a faster rate than precipitation, such that as measured by precipitation minus evaporation ($P - E$), the Sahel actually dries; c48-HiRAM is the only model in which $P - E$ increases. Of the 14 models in which total precipitation decreases, evapotranspiration increases slightly in MIROC5 and NCAR-CCSM4, and potential evapotranspiration increases in all GFDL models and in 5 of the 10 CMIP5 models. All other hydroclimatic responses in all models signify drying. This robust drying response to uniform SST warming stands in sharp contrast to the wide spread

TABLE 3. Sahel region-mean surface hydrological cycle fields in the GFDL model control simulations and their response per unit of imposed SST warming in the +2-K simulations. Values in the top row are from the CRU TS v4.01 observational dataset averaged over 1980–2005. The remaining rows are the control simulation values from the GFDL models, with the perturbation values in parentheses per unit of imposed SST warming. Columns, from left to right, are total precipitation, convective precipitation, large-scale precipitation, precipitation minus evapotranspiration, evapotranspiration, potential evapotranspiration (all in mm day^{-1}), relative humidity at 925 hPa (%), and surface air temperature (K). Models are ordered from top to bottom based on their total precipitation response, from most negative to most positive.

	P	P_{conv}	P_{ls}	$P - E$	E	E_{pot}	$\text{RH}_{925\text{hPa}}$	T_{sfc}
CRU	3.0	—	—	—	—	—	—	303.2
Ensemble mean	3.4 (−0.19)	2.6 (−0.13)	0.8 (−0.07)	1.1 (−0.17)	2.3 (−0.03)	2.8 (+0.06)	56.8 (−1.89)	302.7 (+1.69)
AM2.1	3.8 (−0.67)	3.6 (−0.61)	0.2 (−0.07)	1.4 (−0.49)	2.3 (−0.19)	3.0 (+0.06)	60.3 (−4.79)	300.8 (+2.27)
AM2.5	4.6 (−0.49)	4.2 (−0.44)	0.5 (−0.05)	2.0 (−0.42)	2.6 (−0.07)	3.0 (+0.04)	65.4 (−2.39)	301.7 (+1.77)
c90-AM3	3.5 (−0.30)	3.3 (−0.24)	0.2 (−0.06)	0.8 (−0.24)	2.7 (−0.06)	3.1 (+0.03)	54.7 (−2.64)	303.4 (+1.94)
AM3	2.8 (−0.20)	2.5 (−0.08)	0.2 (−0.12)	0.4 (−0.05)	2.3 (−0.14)	2.8 (+0.02)	47.7 (−1.44)	305.0 (+1.76)
c180-HiRAM	3.9 (+0.02)	0.7 (+0.08)	3.2 (−0.06)	1.8 (−0.02)	2.1 (+0.04)	2.8 (+0.05)	62.8 (−0.79)	302.8 (+1.42)
AM2.1-UW	2.7 (+0.10)	1.9 (+0.22)	0.8 (−0.12)	0.3 (−0.05)	2.4 (+0.15)	2.7 (+0.15)	56.3 (−1.79)	299.4 (+1.39)
c48-HiRAM	2.5 (+0.19)	1.7 (+0.20)	0.7 (−0.01)	0.9 (+0.09)	1.6 (+0.09)	2.5 (+0.06)	50.1 (+0.63)	305.4 (+1.22)

in models noted previously in coupled future emissions scenario simulations and to the robust increase in precipitation in fixed-SST simulations with quadrupled CO_2 (Gaetani et al. 2017).

As expected, surface warming is generally larger in models in which the drying is stronger. Robust decreases in large-scale precipitation seem straightforwardly linked to reduced relative humidity. In most models, that potential evapotranspiration increases while evapotranspiration decreases can be interpreted through supply-limited evaporative dynamics: when precipitation is sufficiently low, evapotranspiration is limited not by atmospheric demand but by the supply of moisture to the soil by precipitation (e.g., Roderick et al. 2014; Lintner et al. 2015). This also provides a straightforward explanation for the increase in evapotranspiration in the three UW convection models, in which total precipitation also increases. Note, however, that these purely supply-limited arguments are imperfect: in most models precipitation is not substantially smaller than potential evapotranspiration (cf. Tables 3 and 4), indicating an intermediate regime in which evapotranspiration can be sensitive both to moisture supply by precipitation and atmospheric demand.

Figure 3a shows the Sahel region-mean precipitation change in each model (Fig. 3b will be discussed in section 4). The precipitation responses per unit of imposed SST warming span a larger range across the GFDL models than across the CMIP5 models, but this stems partly from the difference in the imposed SST warming (+2 K for GFDL, +4 K for CMIP5). The unfilled markers overlaid for AM2.1, AM3, and AM2.1-UW are the responses per unit imposed SST warming in uniform 4-K SST warming simulations performed in those models, and they span a narrower range than the corresponding

+2-K simulations (although still wider than that of the 10 CMIP5 models). As described by H17, the Sahel rainfall response in AM2.1 “saturates” as SSTs are warmed beyond roughly 1 K (cf. Fig. 13b of H17), but in AM2.1-UW it remains linear with the imposed SST change from the control to at least a 6-K warming (cf. Fig. 14b of H17). We have replicated a subset of these simulations in AM3 (not shown); like AM2.1, the Sahel rainfall response essentially saturates as SSTs are warmed beyond 1 K. Thus, it is reasonable to suspect that at least some of the CMIP5 models would likewise exhibit stronger Sahelian drying per unit imposed SST warming were they subjected to smaller magnitude warming, although we lack a means of predicting which models and by how much. Despite this difference in spread within either ensemble, the two ensemble-mean responses are nearly identical (−0.19 and −0.18 $\text{mm day}^{-1} \text{K}^{-1}$ for GFDL and CMIP5, respectively).

4. GFDL and CMIP5 model MSE budget responses to uniform SST warming

Given that Sahelian precipitation decreases in 14 of the 17 models (increasing only in the closely related GFDL model variants all using the UW scheme), we now attempt to determine if that drying arises from the mechanism posited by H17. Specifically, we analyze the Sahel region-mean vertical profiles of the MSE advection terms as well as the column-integrated source term (i.e., the TOA radiative fluxes). The H17 mechanism would be evinced by an increased meridional MSE gradient, anomalous export of MSE through meridional advection, anomalous subsidence in the free troposphere, and a weak response in the TOA radiative

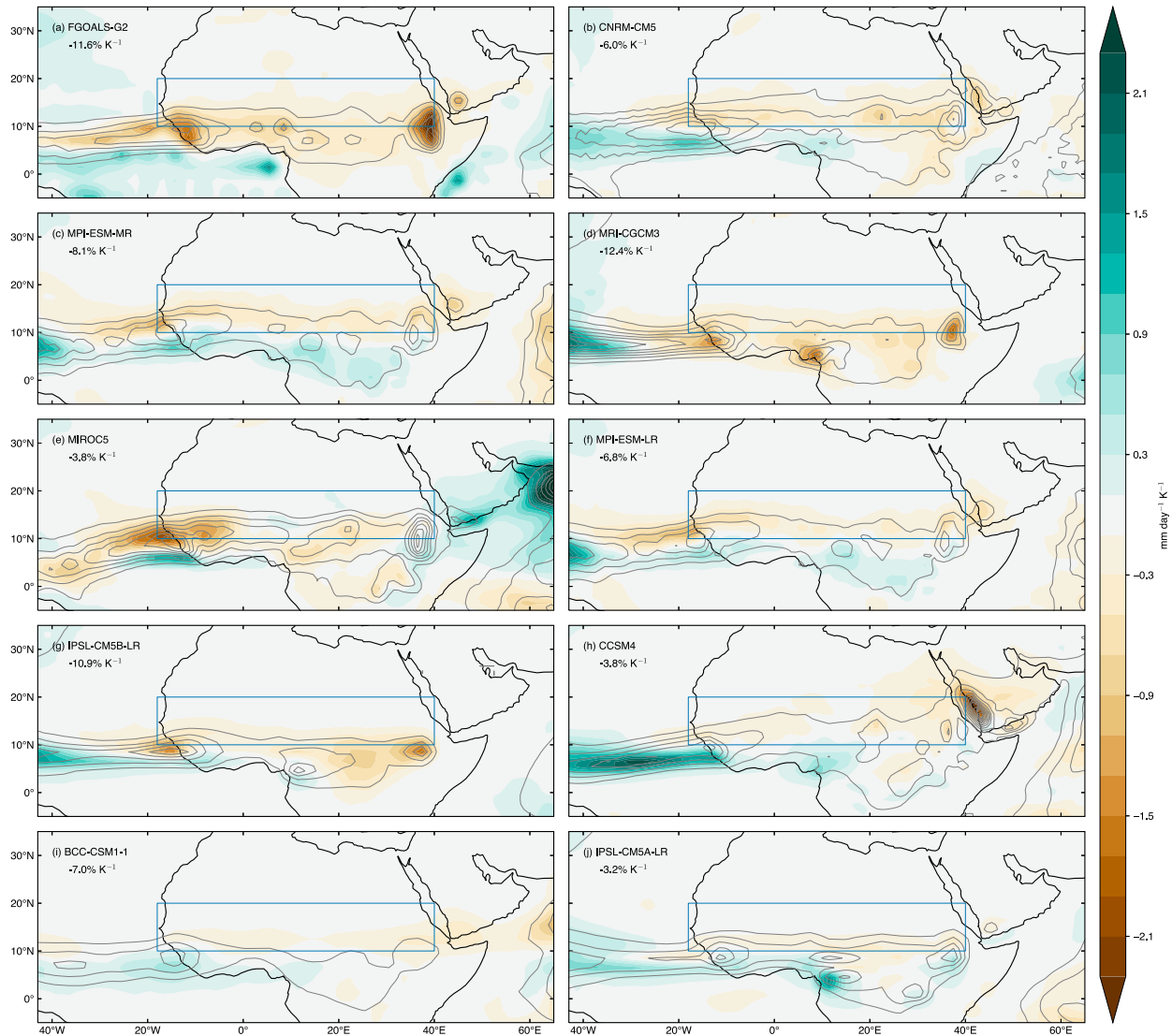


FIG. 2. As in Figs. 1a–g, but for the 10 CMIP5 models, and for 4-K rather than 2-K warming.

flux. We will show that all but the last of these hold in every model analyzed.

a. Horizontal advection

Figure 4 shows the control and perturbation Sahel region-mean profiles of meridional wind, meridional MSE gradient, and horizontal (meridional plus zonal) MSE advection in the GFDL models; Fig. 5 shows the same for the CMIP5 models. Figures S1 and S2 in the online supplemental material show the same but with the meridional (rather than meridional plus zonal) MSE advection profiles.

The first-order behavior in the control simulations is consistent across all models. The meridional wind is generally southerly in the boundary layer, upper troposphere,

and stratosphere and northerly in the lower and middle free troposphere (Figs. 4a and 5a). The meridional MSE gradient is negative (i.e., MSE decreases moving northward) at nearly all levels, with the largest values in the lower troposphere (Figs. 4b and 5b). MSE divergence through horizontal advection peaks in the lower troposphere and steadily decreases toward zero in the middle to upper troposphere (Figs. 4c and 5c).

In response to uniform SST warming, meridional wind responds differently in different models with generally weak magnitudes, at most $\pm 0.3 \text{ m s}^{-1} \text{ K}^{-1}$ at any tropospheric level (Figs. 4d and 5d). In contrast, the prevailing meridional MSE gradient increases in magnitude over most or all of the troposphere in all models (Figs. 4e and 5e). Combined, horizontal MSE advection primarily

TABLE 4. As in Table 3, but for the CMIP5 models.

	P	P_{conv}	P_{ls}	$P - E$	E	E_{pot}	$\text{RH}_{925\text{hPa}}$	T_{sfc}
CRU	3.0	—	—	—	—	—	—	303.2
Ensemble mean	2.8 (−0.18)	2.2 (−0.12)	0.6 (−0.07)	1.1 (−0.13)	1.7 (−0.05)	3.0 (+0.03)	52.0 (−1.71)	302.4 (+1.62)
FGOALS-g2	2.6 (−0.30)	2.0 (−0.18)	0.6 (−0.12)	0.8 (−0.16)	1.8 (−0.14)	3.1 (−0.00)	50.2 (−3.57)	302.5 (+2.00)
CNRM-CM5	4.5 (−0.27)	3.7 (−0.17)	0.8 (−0.10)	2.2 (−0.27)	2.3 (−0.00)	2.6 (+0.06)	63.7 (−2.04)	300.5 (+1.61)
MPI-ESM-MR	2.8 (−0.23)	2.4 (−0.15)	0.5 (−0.09)	1.4 (−0.16)	1.5 (−0.07)	3.0 (+0.03)	51.0 (−2.14)	303.5 (+1.71)
MRI-CGCM3	1.7 (−0.20)	1.5 (−0.19)	0.2 (−0.02)	0.2 (−0.06)	1.4 (−0.14)	2.7 (−0.03)	41.9 (−1.99)	304.7 (+1.79)
MIROC5	5.1 (−0.20)	3.0 (−0.12)	2.1 (−0.08)	2.9 (−0.21)	2.2 (+0.01)	3.4 (+0.04)	57.2 (−0.80)	303.4 (+1.32)
MPI-ESM-LR	2.6 (−0.18)	2.2 (−0.12)	0.4 (−0.06)	1.3 (−0.14)	1.3 (−0.04)	2.9 (+0.04)	50.3 (−1.74)	303.8 (+1.69)
IPSL-CM5B-LR	1.3 (−0.14)	1.1 (−0.11)	0.1 (−0.03)	0.1 (−0.04)	1.2 (−0.10)	3.4 (−0.10)	39.4 (−1.22)	301.7 (+1.57)
NCAR-CCSM4	3.6 (−0.14)	2.4 (−0.01)	1.2 (−0.13)	1.3 (−0.15)	2.3 (+0.01)	2.5 (+0.01)	69.0 (−1.44)	299.3 (+1.51)
BCC-CSM1	1.3 (−0.09)	1.0 (−0.05)	0.3 (−0.04)	0.1 (−0.03)	1.1 (−0.06)	2.6 (−0.06)	47.0 (−1.70)	302.9 (+1.64)
IPSL-CM5A-LR	2.6 (−0.08)	2.5 (−0.07)	0.1 (−0.02)	0.9 (−0.08)	1.7 (−0.01)	3.5 (−0.01)	50.5 (−0.43)	302.0 (+1.38)

responds with anomalous MSE divergence, especially in the middle and lower free troposphere (Figs. 4f and 5f). Of the GFDL models, AM2.1 has the strongest enhancement of the meridional MSE gradient over most of the free troposphere.

Variations in Sahel rainfall are often thought to be determined by variations in the strengths of local meridional overturning circulations, both the West African monsoon and the shallow, dry “Sahara heat low” circulation (e.g., Evan et al. 2015; Gaetani et al. 2017). A relationship does exist in the GFDL models between the vertical structure of their meridional wind responses and their precipitation responses: the Sahel dries more in models such as AM2.1 in which the wind anomaly is

more northerly in the lower troposphere and more southerly in the upper troposphere (Fig. 4d). However, at least in AM2.1, near-surface northerly anomalies are in fact partly a response to surface warming driven by the reduced evaporative cooling (H17). There is also no discernible link between the two fields in the CMIP5 models (Fig. 5d)—a discrepancy between the ensembles we do not understand. Also, note that the depth of the anomalous northerlies suggests, if anything, a link to the deep, moist circulation rather than the dry, shallow, heat-low circulation (cf. Shekhar and Boos 2017; Zhai and Boos 2017).

In most models the meridional MSE advection dominates the total (compare Figs. 4c,f to Figs. S1c,f, and

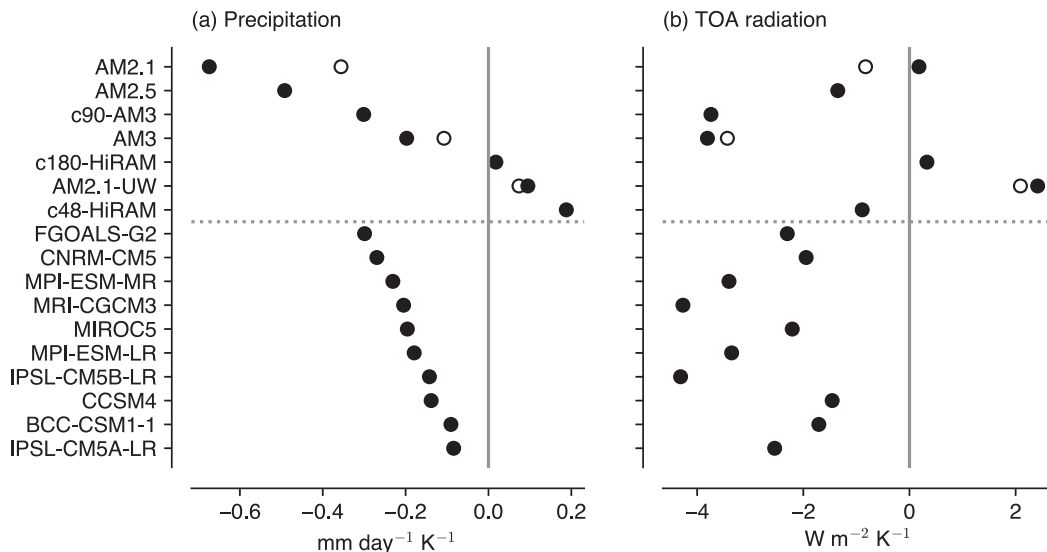


FIG. 3. Sahel region-mean response per unit of imposed SST warming of (a) precipitation ($\text{mm day}^{-1} \text{K}^{-1}$) and (b) net downward TOA radiative flux ($\text{W m}^{-2} \text{K}^{-1}$). Unfilled markers for AM2.1, AM3, and AM2.1-UW are the values in uniform 4-K SST warming simulations performed in those models. The horizontal dotted gray line separates the GFDL and CMIP5 models. The solid gray vertical line denotes a value of zero. The models are ordered within each ensemble from top to bottom by their region-mean precipitation response, from most to least drying.

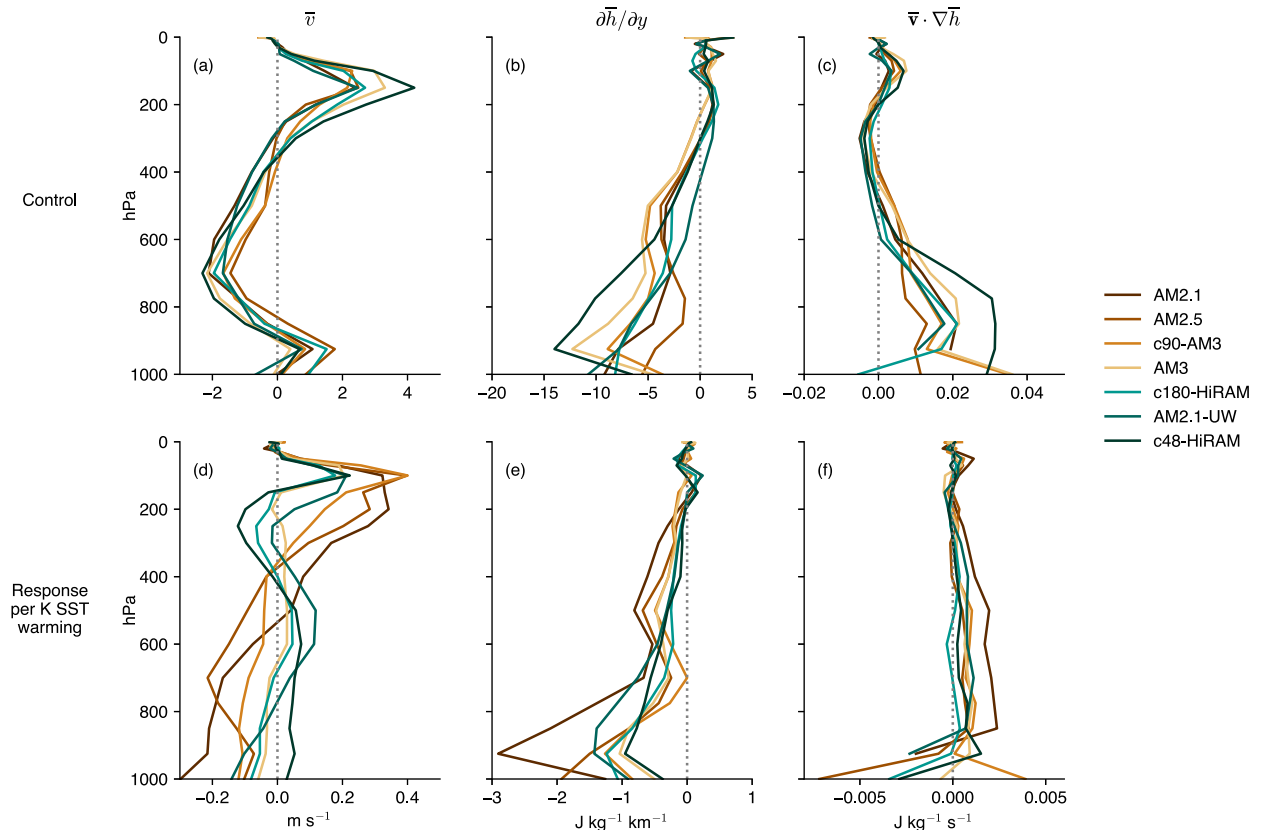


FIG. 4. Sahel region-mean profiles of time-mean (left) meridional wind, (center) meridional MSE gradient, and (right) horizontal MSE advection (positive values correspond to export of MSE) (a)–(c) in the control simulations and (d)–(f) in response to 2-K SST warming in the GFDL models. The color of each curve corresponds to the model’s Sahel region-mean precipitation response per unit of imposed SST warming; the darkest green is the most positive of the GFDL models, and the darkest brown is the most negative of the GFDL models. Note the smaller horizontal axis spacing in (d)–(f).

Figs. 5c,f to Figs. S2c,f), especially from the surface through the midtroposphere. Figures S3 and S4 show the corresponding zonal advection terms in the GFDL and CMIP5 models, respectively. Most models simulate easterlies over the whole free troposphere, including an African easterly jet in the midtroposphere, and modest westerlies within the boundary layer, but the zonal MSE gradients vary across models such that zonal MSE advection is not of consistent sign across models. The signs of the responses to warming of the zonal wind, MSE gradient, and MSE advection are likewise inconsistent, apart from consistent westerly anomalies above ~ 400 hPa. In particular, there is no obvious link between the responses of the African easterly jet and of precipitation, a claim made frequently in the literature (e.g., Cook 1999; Gaetani et al. 2017).

b. Vertical advection

Figure 6 shows the control and perturbation Sahel region-mean profiles of pressure velocity, moist static

stability, and vertical MSE advection in the GFDL models. Figure 7 shows the pressure velocity profiles for the CMIP5 models (recall that moist static stability and vertical MSE advection were omitted for CMIP5; cf. discussion in section 2d). The first-order behavior in the control simulations is consistent across all models. Compared to the meridional (Figs. 4a and 5a) and zonal (Figs. S3a and S4a) wind, there is more model spread in the ascent profiles (Figs. 6a and 7a), which span from “top-heavy,” with ascent peaking in the upper troposphere (e.g., AM2.5, CNRM-CM5), to “bottom-heavy,” with ascent peaking below 800 hPa (e.g., AM2.1-UW, NCAR-CCSM4). The moist static stability profiles have comparatively little spread, with $\partial_p h > 0$ in the lower troposphere and $\partial_p h < 0$ in the upper troposphere, reflecting a first-baroclinic-mode MSE structure typical of low latitudes (Fig. 6b). As a result, vertical advection generally converges MSE in the lower free troposphere and diverges it aloft (Fig. 6c).

In response to SST warming, all models simulate a shallowing of the ascent profile as noted by H17 for

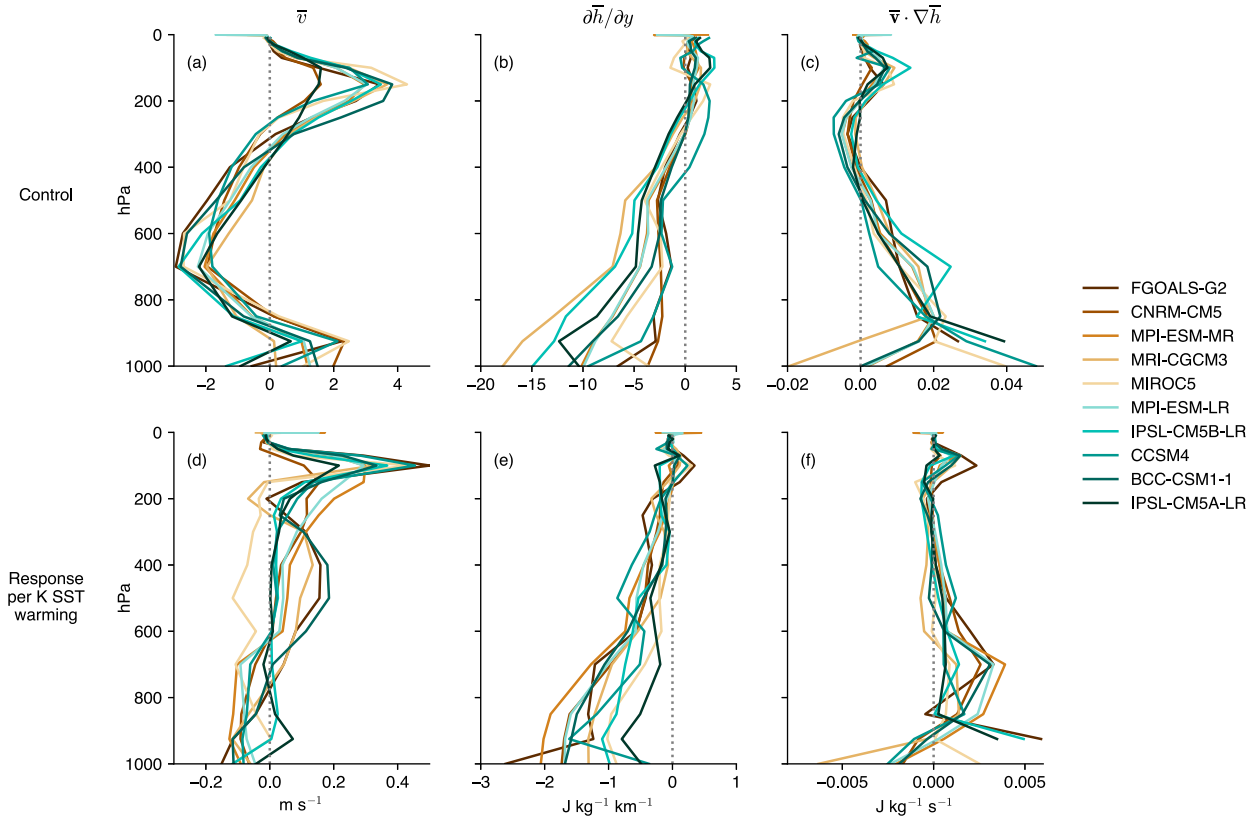


FIG. 5. As in Fig. 4, but for the CMIP5 models under 4-K warming.

AM2.1 and AM2.1-UW, with anomalous descent over much of the free troposphere overlying anomalous ascent near the surface (Figs. 6d and 7b). Responses of moist static stability are much more similar across the GFDL models, generally modestly enhancing and shifting upward the climatological profile. Combined, the circulation shallowing generally controls the vertical advection response, with anomalous MSE import throughout much of the free troposphere in most models (Fig. 6f).

Analysis of the convective mass flux profiles in the GFDL models (except for c90-AM3 and AM2.1-UW, for which the field was inadvertently not saved) reveals that, like the ascent profiles, the mass flux profiles span a wide range in both the control and the response to SST warming (Fig. S5). Of particular note, in both HiRAM variants (and, we suspect, in AM2.1-UW), the convective mass flux *increases* over a majority of the free troposphere. Thus, the UW convection scheme is apparently invigorated by the overall warming. All else being equal, the increase in evapotranspiration in these models would promote moist convection, but in a semiarid region this is better considered a response to the precipitation change rather than a forcing. Moreover, as documented in H17 for AM2.1-UW (see their Fig. 14), the region dries by

essentially every other measure. The hypothesis set forth by H17 regarding the UW parameterization based on Zhao (2014) remains plausible and worth further study: the UW scheme represents the fractional lateral mixing rate as being inversely proportional to the convective depth. As the climate warms and convective depth tends to increase (e.g., Singh and O’Gorman 2012), this acts to decrease the lateral mixing, invigorating the parameterized convection.

c. Net energetic forcing and its components

Tables 5 and 6 list the control simulation net energetic forcing term and the contributions thereto from the clear-sky TOA radiative flux and net, shortwave (SW), and longwave (LW) TOA cloud radiative effect (CRE; recall that this is the difference between the all-sky and clear-sky values) for the GFDL and CMIP5 ensembles, respectively, as well as the observational estimate from CERES-EBAF. The models bracket the observed all-sky TOA radiation of 45.8 W m^{-2} , ranging from 20.1 W m^{-2} (MRI-CGCM3) to 61.3 W m^{-2} (AM2.5), and likewise for the clear-sky (39.2 W m^{-2} in CERES-EBAF; from 20.5 W m^{-2} in MRI-CGCM3 to 67.7 W m^{-2} in CNRM-CM5). But the net CRE is less positive than the CERES-EBAF value of $+6.6 \text{ W m}^{-2}$ in all but one model

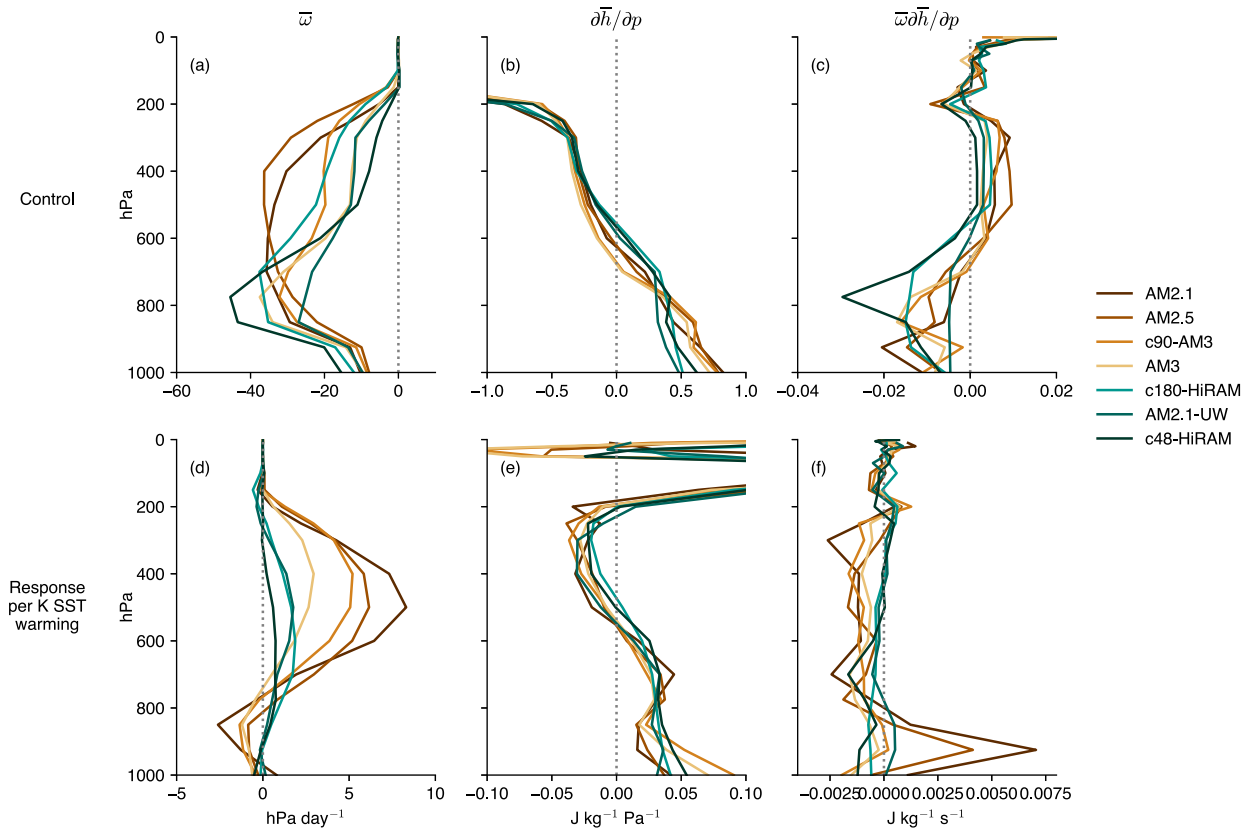


FIG. 6. For the GFDL models, Sahel region-mean profiles of (left) pressure velocity, (center) moist static stability, and (right) vertical MSE advection (positive values correspond to export of MSE) in (a)–(c) the control simulations and (d)–(f) their responses per 1 K of imposed SST warming. Note the smaller horizontal axis spacing in (d)–(f). Colors are as in Fig. 4.

(IPSL-CM5A-LR, $+12.1 \text{ W m}^{-2}$), with the lowest value of -28.7 W m^{-2} in NCAR-CCSM4. Only two models (high is 40.5 W m^{-2} , AM2.5) have LW CRE higher than the CERES-EBAF value of 38.7 W m^{-2} (low is 14.2 W m^{-2} , IPSL-CM5B-LR), while 11 models are more negative and six models less negative than the CERES-EBAF -32.1 W m^{-2} value for SW CRE (-66.0 W m^{-2} in NCAR-CCSM4 to -10.4 W m^{-2} in IPSL-CM5B-LR). The ensemble-mean net CRE differences versus CERES-EBAF are similar (-15.2 and -12.8 W m^{-2} for GFDL and CMIP5, respectively), with similar contributions from LW and SW for GFDL but predominantly from LW CRE for CMIP5.⁶

⁶ In GCMs, CRE and clear-sky fluxes are computed from the all-sky flux by repeating the radiative transfer calculation with all clouds removed, but with the temperature and moisture soundings otherwise the same. In the satellite observations, this partitioning is computed based on conditional sampling of pixels with and without clouds, which can lead to biases (X. Huang 2018, personal communication). This may therefore lead to a secular difference between the modeled and observational values.

Figure 3b shows the region-mean net TOA radiative flux response in all models; recall that this is equivalent to the net energetic forcing for a land region. The energetic forcing responds weakly in AM2.1 and c180-HiRAM ($+0.18$ and $+0.33 \text{ W m}^{-2} \text{ K}^{-1}$, respectively) and increases in AM2.1-UW ($+2.42 \text{ W m}^{-2} \text{ K}^{-1}$). In the other 14 models, it decreases appreciably, by up to $4.31 \text{ W m}^{-2} \text{ K}^{-1}$ in IPSL-CM5B-LR. In fact, the weak energetic forcing response is unique even in AM2.1 to the +2-K simulation; in the +4-K simulation in AM2.1, the forcing term does become appreciably more negative [see also Fig. 13(i) of H17], as indicated by the overlaid +4-K simulation values in Fig. 3b. So, for the drying models other than AM2.1, the anomalous dry advection is balanced partly by reduced energetic forcing, necessitating less anomalous descent than if the TOA radiative response was weak as in AM2.1 (or positive).

Tables 5 and 6 also list the perturbation values of these TOA fluxes. In AM2.1, the weak change in net TOA radiative flux with SST warming arises from cancellation between reduced clear-sky radiation ($-4.79 \text{ W m}^{-2} \text{ K}^{-1}$)

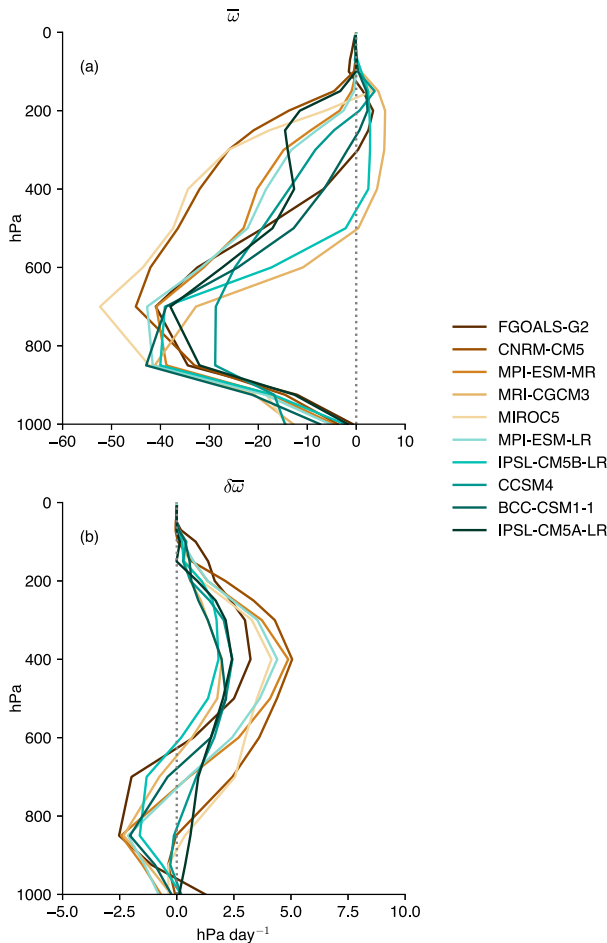


FIG. 7. For the CMIP5 models, Sahel region-mean profiles of pressure velocity in (a) the control simulations and (b) their responses per 1 K of imposed SST warming. Note the smaller horizontal axis spacing in (b). Colors are as in Fig. 5. Because of data availability constraints described in section 2d, moist static stability and vertical MSE advection are omitted for CMIP5.

and increased net CRE ($+4.97 \text{ W m}^{-2} \text{ K}^{-1}$), the latter driven primarily by decreased cloudy-sky SW reflectance (i.e., increased SW CRE, $+6.69 \text{ W m}^{-2} \text{ K}^{-1}$), counteracted slightly by increased cloudy-sky OLR (i.e., decreased LW CRE, $-1.72 \text{ W m}^{-2} \text{ K}^{-1}$). Across all models, clear-sky net TOA radiation almost necessarily decreases (-0.96 to $-4.79 \text{ W m}^{-2} \text{ K}^{-1}$), as the warmed surface and troposphere emit more LW radiation that escapes to space. Shallowing of moist convection and concomitant cloud loss cause the LW CRE to become less positive in all models except c180-HiRAM (-3.33 to $+0.49 \text{ W m}^{-2} \text{ K}^{-1}$) and the SW CRE to become more positive in all models ($+0.63$ to $+6.69 \text{ W m}^{-2} \text{ K}^{-1}$). The LW and SW relative magnitudes vary, such that the net CRE response is not of consistent sign (-1.12 to $+5.04 \text{ W m}^{-2} \text{ K}^{-1}$), although averaged within either ensemble it is positive ($+1.69$ and $+0.36 \text{ W m}^{-2} \text{ K}^{-1}$ for

GFDL and CMIP5, respectively). Combining the robustly negative clear-sky net TOA radiative flux with the mixed response of net CRE yields the reduced all-sky TOA radiative flux into the Sahel in all models except AM2.1, c180-HiRAM, and AM2.1-UW described above.

5. Toward an emergent observational constraint

H17 speculate that if the climatological convection in the Sahel is especially deep, then the meridional MSE difference between the Sahel and Sahara will be enhanced over a greater depth with SST warming, and therefore the column-integrated anomalous dry advection, compensating subsidence, and precipitation reduction will all be stronger. Restricting to the GFDL models, the above results lend qualitative support to this picture: precipitation is generally reduced more in models with greater subsidence anomalies (Fig. 6d), greater enhancement of the meridional MSE gradient in the middle and upper troposphere (Fig. 4e), and more top-heavy climatological ascent (Fig. 6a). It is thus worthwhile to quantify these relationships in both sets of models and across all of them.

The first step in this causal chain is a positive covariance between anomalous precipitation and anomalous descent. Figure 8 shows the responses of precipitation and ω at 500 hPa per 1 K of SST warming for each GFDL and CMIP5 model (results are similar at adjacent pressure levels or averaged over the midtroposphere; not shown). For the GFDL models, the precipitation response is almost perfectly anticorrelated ($r = -0.98$) with the anomalous midtropospheric subsidence, as expected: insofar as the Sahel is close enough to the equator for weak temperature gradient dynamics to govern free-tropospheric motions, precipitation and vertical velocities are tightly linked (Emanuel et al. 1994). However, for the CMIP5 models the linear relationship is much weaker, $r = -0.55$ and with an appreciably shallower slope. Though the combined ensemble exhibits a large correlation of $r = -0.90$, the different slopes and correlation coefficients imply that the statistics of the combined single 17-member distribution may not be physically meaningful. Also, if fractional rather than absolute precipitation responses are used, the anticorrelation for GFDL remains nearly perfect ($r = -0.99$), but for the CMIP5 models the sign of the correlation reverses, $r = +0.53$ (not shown).

This difference between the ensembles does not appear to stem purely from the difference in the imposed SST warming magnitude discussed previously. Overlaid on Fig. 8 are the values from the +4-K simulations in AM2.1, AM3, and AM2.1-UW and the best-fit line to this three-member distribution. Though the responses

TABLE 5. Sahel region-mean net top of atmosphere (TOA) radiative flux and its components (all in W m^{-2}) and signed positive into the atmosphere. Values in the top row are from the CERES-EBAF v4.0 observational dataset averaged over 2000–17. The remaining rows are the values from the GFDL models, with the multimodel mean values in the second row and values for individual models in subsequent rows. Control simulation values are listed with the perturbation values per unit of imposed SST warming ($\text{W m}^{-2} \text{K}^{-1}$) in parentheses. Columns, from left to right, are all-sky TOA radiative flux, clear-sky TOA radiative flux, cloud radiative effect (CRE), shortwave CRE, and longwave CRE.

	TOA rad	TOA rad, clear	Net CRE	SW CRE	LW CRE
CERES-EBAF	45.8	39.2	6.6	−32.1	38.7
Ensemble mean	47.5 (−0.98)	56.2 (−2.67)	−8.6 (+1.69)	−40.8 (+3.15)	32.2 (−1.46)
AM2.1	54.5 (+0.18)	62.6 (−4.79)	−8.4 (+4.97)	−39.3 (+6.69)	31.2 (−1.72)
AM2.5	61.3 (−1.35)	64.5 (−2.43)	−3.2 (+1.08)	−43.7 (+2.76)	40.5 (−1.67)
c90-AM3	55.1 (−3.74)	50.2 (−3.74)	5.0 (−0.00)	−34.4 (+3.26)	39.4 (−3.26)
AM3	48.6 (−3.81)	43.2 (−2.85)	5.5 (−0.96)	−26.4 (+0.87)	31.9 (−1.82)
c180-HiRAM	40.4 (+0.33)	58.3 (−1.30)	−17.8 (+1.63)	−45.7 (+1.14)	27.9 (+0.49)
AM2.1-UW	34.8 (+2.42)	62.3 (−2.42)	−27.6 (+5.04)	−56.2 (+6.57)	28.7 (−1.54)
c48-HiRAM	37.9 (−0.89)	52.1 (−0.96)	−14.2 (+0.07)	−39.5 (+0.75)	25.3 (−0.68)

per unit of SST warming of both ω and precipitation change appreciably going from +2 to +4 K (particularly for AM2.1), they still obey the same linear relationship as in the +2-K simulations: the best-fit line for these three +4-K simulations is nearly identical to that of the seven-member GFDL +2-K ensemble. This is in contrast to the spread within either ensemble in the precipitation response, for which the magnitude of the imposed SST warming does matter (section 3).

We do not fully understand why the CMIP5 and GFDL ensembles exhibit differing quantitative relationships among the various fields presented. As another example, while the evapotranspiration and precipitation responses to SST warming are highly correlated across the GFDL models ($r = 0.95$), in the CMIP5 models there is effectively no relationship between the two fields ($r = 0.09$; not shown). A tight correspondence between evapotranspiration and precipitation is one of the hallmarks of semiarid regions. However, we have experimented with excluding certain models based on such appeals to physical intuition and have not found correlations to be easily improved.

Hill (2016, chapter 4) examines all of the fields of potential relevance to our theory—horizontal MSE advection, vertical MSE advection, and the various radiative fluxes. Although essentially all of them qualitatively adhere to the dynamical arguments posed above (particularly for the GFDL models), for the combined ensemble the aforementioned midtropospheric ω response is the only one with a statistically significant correlation to the precipitation response. We offer potential means of extending these analyses relating to an emergent constraint in the discussion section (section 7) below.

6. Relationships between precipitation and cloud radiative properties

Section 4c showed that, of the 14 models in which the Sahel-mean precipitation decreases with uniform SST warming, AM2.1 is the only one in which the region-mean TOA radiative forcing does not also decrease. Moreover, this weak net radiative response is the result of canceling clear-sky and CRE responses. In this section, we seek to determine the physical plausibility of

TABLE 6. As in Table 5, but for the CMIP5 models.

	TOA rad	TOA rad, clear	Net CRE	SW CRE	LW CRE
CERES-EBAF	45.8	39.2	6.6	−32.1	38.7
Ensemble mean	39.0 (−2.75)	45.2 (−3.11)	−6.2 (+0.36)	−35.3 (+2.34)	29.1 (−1.97)
FGOALS-G2	27.2 (−2.30)	45.4 (−4.23)	−18.1 (+1.93)	−42.9 (+3.50)	24.8 (−1.57)
CNRM-CM5	54.3 (−1.95)	67.7 (−2.97)	−13.4 (+1.03)	−44.1 (+2.71)	30.7 (−1.69)
MPI-ESM-MR	47.1 (−3.40)	44.5 (−3.71)	2.5 (+0.31)	−31.1 (+3.59)	33.6 (−3.28)
MRI-CGCM3	20.1 (−4.27)	20.5 (−3.15)	−0.3 (−1.12)	−23.1 (+0.22)	22.7 (−1.35)
MIROC5	50.7 (−2.21)	63.3 (−1.69)	−12.6 (−0.52)	−43.7 (+1.05)	31.1 (−1.58)
MPI-ESM-LR	47.2 (−3.35)	44.4 (−3.19)	2.8 (−0.16)	−33.1 (+3.17)	35.9 (−3.33)
IPSL-CM5B-LR	33.2 (−4.31)	29.3 (−3.57)	3.8 (−0.74)	−10.4 (+0.63)	14.2 (−1.37)
NCAR-CCSM4	28.3 (−1.46)	57.0 (−3.46)	−28.7 (+2.00)	−66.0 (+4.67)	37.3 (−2.67)
BCC-CSM1	37.4 (−1.71)	47.6 (−2.74)	−10.1 (+1.04)	−43.7 (+2.67)	33.6 (−1.63)
IPSL-CM5A-LR	44.4 (−2.54)	32.3 (−2.38)	12.1 (−0.16)	−14.8 (+1.12)	26.9 (−1.28)

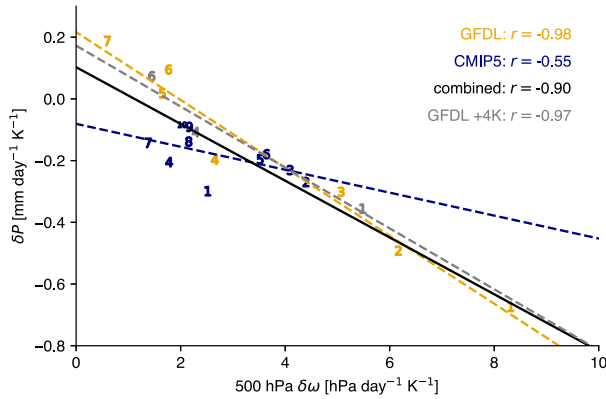


FIG. 8. Scatterplot of Sahel region-mean precipitation change (vertical axis) as a function of ω change at 500 hPa (horizontal axis), both expressed per unit of imposed SST warming ($\text{mm day}^{-1} \text{K}^{-1}$ and $\text{hPa day}^{-1} \text{K}^{-1}$, respectively). Each point corresponds to a single model—gold for GFDL and blue for CMIP5—and with the number corresponding to the Sahel precipitation response ranking within that ensemble, with numbers increasing from most negative to most positive (cf. Tables 3 and 4). The color and text with the corresponding curve are the best-fit line and correlation coefficient for that ensemble. The black line and text are the linear best fit for the combined GFDL and CMIP5 data. Gray points, line, and text correspond to the +4-K SST simulations performed in AM2.1, AM3, and AM2.1-UW.

these radiative responses through examining their interannual counterparts in a subset of models and in observations. We then assess whether the interannual behavior can be linked to the equilibrium responses to imposed SST warming.

We compute annual time series of Sahel region-mean JAS TOA radiative fields using CERES-EBAF, precipitation using CRU TS (both over their common period of 2000–16), and of both fields over the full durations of the “extended AMIP” simulations in AM2.1

and AM3 and in the standard AMIP simulation in c180-HiRAM described in section 2f. In all cases, we remove any long-term linear trend before comparing across variables, although this has little impact on the results (not shown). We also subtract the time mean of each field, in order to present values in terms of deviations from the long-term average. Note that the comparisons between observations and models are made imperfect by the fact that CERES data do not overlap at all with the AM2.1 simulation, and in the AM3 and c180-HiRAM simulations for only 2000–05 and 2000–08, respectively.

Figure 9 shows the relationships between Sahel precipitation and the net all-sky TOA radiative flux in the observations and in each model. The observations and AM3 adhere to classical expectations (e.g., Neelin and Held 1987): precipitation and TOA radiative flux covary positively [3.6 and $8.1 \text{ W m}^{-2} (\text{mm day}^{-1})^{-1}$, respectively]. But in c180-HiRAM, there is effectively no relationship, and in AM2.1 drier years are actually associated with greater net forcing of the column [$-3.0 \text{ W m}^{-2} (\text{mm day}^{-1})^{-1}$].

Figure 10 decomposes this all-sky radiative flux into clear-sky and cloudy-sky components. The relationships between rainfall and clear-sky downward TOA flux are fairly consistent across models and observations: the observations, AM2.1, AM3, and c180-HiRAM have slopes of 4.7 , 4.5 , 8.5 , and $5.3 \text{ W m}^{-2} (\text{mm day}^{-1})^{-1}$, respectively (Figs. 10a–d). This is likely due to water vapor: years with more precipitation plausibly have more water vapor under clear-sky conditions, increasing clear-sky LW absorption. Conversely, the observed net CRE becomes slightly less positive as rainfall increases, at $-1.1 \text{ W m}^{-2} (\text{mm day}^{-1})^{-1}$, but the relationship is not strong enough to be statistically significant ($r^2 = 0.10$,

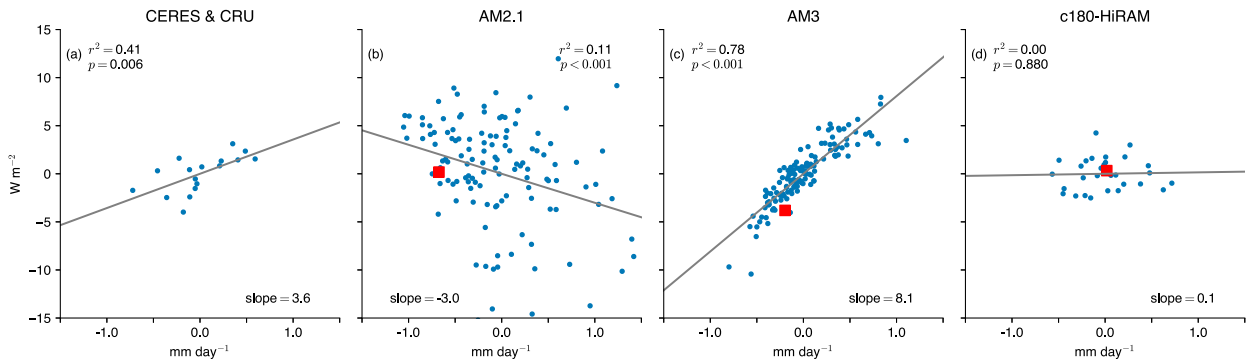


FIG. 9. Sahel region-mean net all-sky TOA radiation (W m^{-2} ; vertical axis) as a function of precipitation (mm day^{-1} ; horizontal axis) in (a) CERES-EBAF and CRU observational data, and AMIP simulations in (b) AM2.1, (c) AM3, and (d) c180-HiRAM. Each dot represents a single year, and the overlaid gray line is the linear best fit. Also printed in each panel is the square of the Pearson correlation coefficient r^2 , the corresponding p value based on a two-sided Student’s t test assuming each year is independent, and the slope of the best-fit line [$\text{W m}^{-2} (\text{mm day}^{-1})^{-1}$]. Red squares in (b) and (c) denote the equilibrium response in the uniform 2-K SST warming simulation in mm day^{-1} (not normalized by the SST warming).

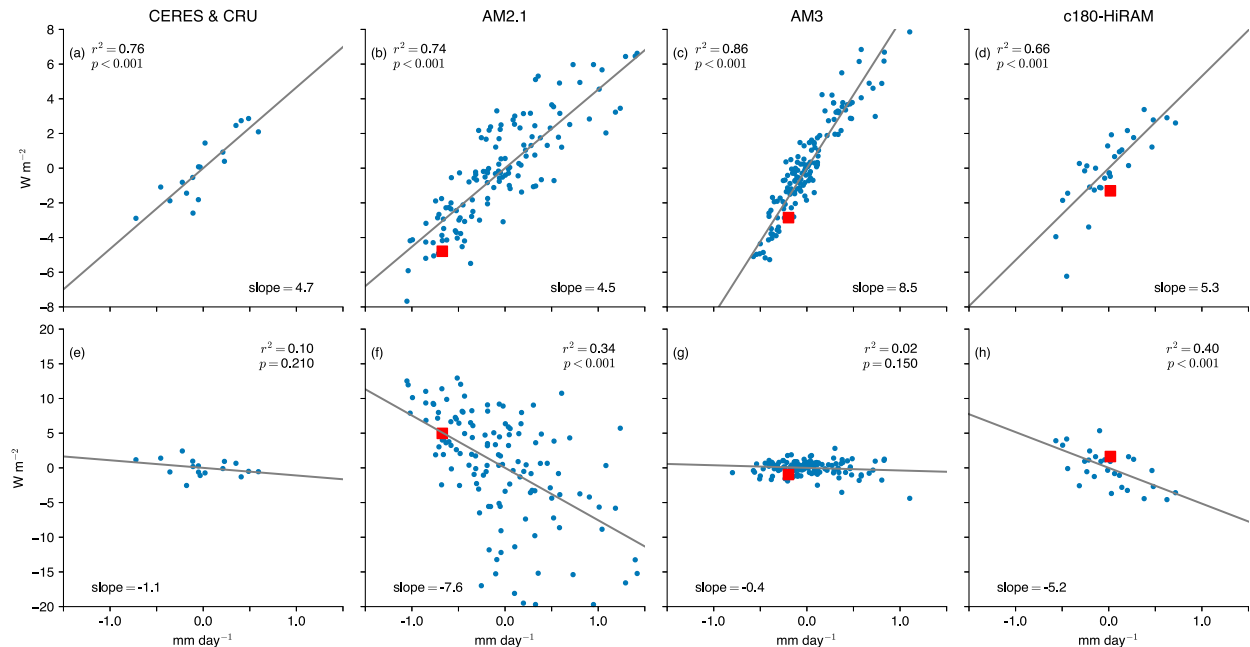


FIG. 10. As in Fig. 9, but with (a)–(d) net clear-sky TOA radiative flux and (e)–(h) net cloud radiative effect as the vertical axis, signed positive into the atmosphere. Note different vertical axis spacing in each row.

$p = 0.21$ based on a two-sided Student's t test and treating each year as independent) (Fig. 10e). The CRE-precipitation slope values are -7.6 , -0.4 , and $-5.2 \text{ W m}^{-2} (\text{mm day}^{-1})^{-1}$ in AM2.1, AM3, and c180-HiRAM respectively (Figs. 10f–h). So it is the excessive cloud radiative covariance with precipitation in AM2.1 that causes the all-sky precipitation–TOA radiation relationship to be of the wrong sign compared to observations.⁷

⁷ As a point of theoretical interest, we note that, in AM2.1 and c180-HiRAM, net CRE is negative in the Sahel JAS mean (Table 5) and becomes more negative as precipitation increases at the interannual time scale (Figs. 10f, h), as increased SW shading (Figs. 11f, h) exceeds increased LW trapping (Figs. 11b, d). Given an anomalously wet year, this implies that the concomitant cloud cover increase acts to decrease the net TOA radiative flux, thereby increasing the efficiency of MSE divergence by the divergent circulation, that is, the “effective gross moist stability” (effective GMS) (Bretherton et al. 2006)—or, almost equivalently, the “drying efficiency,” cf. Inoue and Back (2015). The opposite occurs in an anomalously dry year: decreased cloud SW shading exceeds the decreased cloud LW trapping in magnitude, thereby increasing the net TOA radiative flux and decreasing the effective GMS. This may be contrasted with the observations and AM3, in which net CRE is positive in the Sahel JAS mean (Table 5) and covaries insignificantly with precipitation on the interannual time scale, as well as with deep convecting regions, in which cloud LW trapping exceeds cloud SW shading, and therefore growth of convective towers induces a radiative flux convergence that acts against the MSE divergence by the circulation, thereby acting as a positive feedback on convective growth.

Figure 11 decomposes the net CRE into SW and LW components. In all cases, the relationship between the net CRE and precipitation is the residual of canceling positive SW CRE and negative LW CRE relationships (Fig. 11). The observational LW CRE–precipitation slope is $3.5 \text{ W m}^{-2} (\text{mm day}^{-1})^{-1}$ (Fig. 11a), lower than the three models [5.2 , 10.7 , and $5.1 \text{ W m}^{-2} (\text{mm day}^{-1})^{-1}$, respectively] (Figs. 11b–d). The corresponding relationships for SW CRE are $-4.6 \text{ W m}^{-2} (\text{mm day}^{-1})^{-1}$ in the observations and -12.7 , -11.0 , and $-10.3 \text{ W m}^{-2} (\text{mm day}^{-1})^{-1}$ in AM2.1, AM3, and c180-HiRAM, respectively (Figs. 11e–h). So in all three models the SW shading by clouds varies at more than double the rate per unit precipitation change than observations, with AM2.1 the worst by a modest amount. However, the more modest LW slope in AM2.1 and c180-HiRAM causes the net to be severely negative, whereas the LW and SW variations largely cancel in AM3.

Red squares in the model panels of Figs. 9–11 signify the equilibrium response in the +2-K simulations. A negative offset from the interannual values is apparent in the clear sky for all three models and is to be expected, as the globally warmed troposphere emits more LW radiation to space irrespective of the local hydrological state. In AM2.1 and AM3, this offset also appears in the all-sky field, due to the net CRE equilibrium response closely matching the interannual one; in c180-HiRAM the equilibrium net CRE response is

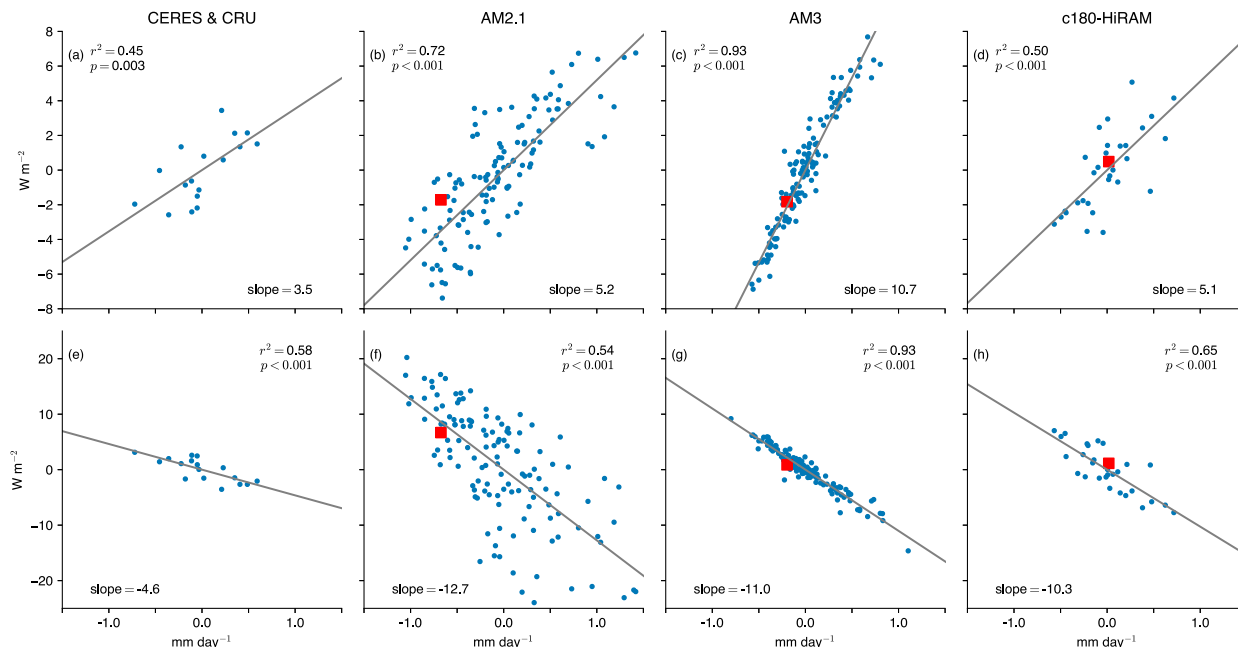


FIG. 11. As in Fig. 9, but with TOA radiation replaced with (a)–(d) longwave and (e)–(h) shortwave cloud radiative effect. Note different vertical axis spacing in each row.

somewhat positively offset. This correspondence provides evidence that the same mechanisms are acting in the forced equilibrium responses and the interannual variability.

For semiarid land regions such as the Sahel, surface evaporative dynamics complicates the influence of cloud radiative variations on precipitation. We have repeated these analyses using surface radiative fluxes from the CERES-EBAF Surface v4.0 observational dataset (Kato et al. 2018); the results are summarized in Fig. S6. The results are similar to the results at TOA in the observations and across models. Thus, in AM2.1, cloud loss allows more radiation to impinge on a surface whose evapotranspiration is moisture limited, thereby warming and reducing the relative humidity of the boundary layer, further inhibiting moist convection (e.g., Derbyshire et al. 2004; Sobel and Bellon 2009; Wang and Sobel 2012).

These arguments suggest two distinct pathways—one at TOA, one at the surface—through which cloud radiative changes in the Sahel feed back positively on drying in AM2.1 in a manner that is excessive compared to observations. We therefore argue that the drying itself is to some extent excessive, although we have not quantified that excess. To a lesser extent, the same would be expected in c180-HiRAM, yet c180-HiRAM's precipitation response to uniform SST warming is weak, consistent with an interpretation that these cloud radiative variations amplify precipitation variations rather than cause them.

7. Discussion

a. Implications of the response to uniform SST warming for the fully coupled response

The end-of-twenty-first-century Sahel rainfall change in the CMIP5 RCP8.5 simulations spans roughly -1 to $+2.5$ mm day^{-1} , with a positive multimodel mean (cf. Fig. 1 of Park et al. 2015). Across all 17 CMIP5 and GFDL AGCMs analyzed, the span of Sahel rainfall responses to uniform SST warming (ignoring the difference in SST warming magnitude) is -1.4 to $+0.4$ mm day^{-1} , or 1.8 mm day^{-1} (i.e., roughly half of the spread in the full twenty-first-century simulation), with a negative multimodel mean. Assuming linearity in the response to uniform SST warming and all other perturbations (Chadwick et al. 2017), the fact that mean SST warming generally dries the Sahel implies that the combined effect of all other twenty-first-century perturbations act to increase precipitation in the Sahel (otherwise the RCP8.5 ensemble would not be appreciably wetter on average than the uniform warming ensemble). This is consistent with prior reports of the general wettening influence in the Sahel of both the pattern of future SSTs (e.g., Park et al. 2015) and of increasing atmospheric CO_2 concentrations (e.g., Dong and Sutton 2015). Gaetani et al. (2017) document a robust *wettening* response in the Sahel in models with fixed SSTs and abruptly quadrupled CO_2 , consistent with the broader impact of increased CO_2 on land precipitation

(Bony et al. 2013), for which vegetation likely plays a meaningful role through stomatal closure (Chadwick et al. 2017).

For example, CM3, the CMIP5 coupled model using AM3 as its atmospheric component, wettens the Sahel in the twenty-first century under the high-emissions RCP8.5 scenario (Fig. 3b of Biasutti 2013), despite AM3's drying response to uniform SST warming. Similarly, the fully coupled version of MIROC responds in the RCP8.5 simulation with the strongest increase in Sahel precipitation across CMIP5 models (Fig. 3b of Biasutti 2013). In models such as these, constraining the effect of mean SST warming evidently does not constrain the full response, unlike in coupled models using AM2.1 (Held et al. 2005). Untangling the roles of mean SST warming, SST spatial pattern changes, and direct forcing on Sahel rainfall remains an outstanding challenge; Chadwick et al. (2017) show that "time slice" simulations may be a valuable tool. Spatial patterns of surface air temperature change over land also generate mechanisms of modifying precipitation over land (Byrne and O'Gorman 2015) that may also need to be considered.

b. Implications for the physical plausibility of AM2.1's projection of severe Sahelian drying

Already established as the "drying-most" outlier in terms of precipitation, these results further highlight AM2.1's peculiarity with respect to the Sahel. Precipitation decreases in the region with +2-K warming more than in any of the other 16 models analyzed, even those subjected to +4-K warming. Yet replacing the default relaxed Arakawa–Schubert convection scheme with the UW scheme causes AM2.1 to go from having the most negative to the second-most positive precipitation response (behind c48-HIRAM) of all models.

AM2.1 is also an outlier in response to climate perturbations in the Tropical Rain Belts with an Annual Cycle and a Continent Model Intercomparison Project (TRACMIP) simulations: from Fig. 11 of Voigt et al. (2016), the precipitation response of an aquaplanet version of AM2.1 to the introduction of a rectangular landmass under solstitial forcing is a severe southward shift of the ITCZ at all latitudes, especially over the continent. This response is an outlier compared to all 12 other models shown.

Nevertheless, we are reluctant to extrapolate these arguments relating to the Sahel to the realism of the hydroclimatic response of AM2.1 in other land regions. The Sahel's proximity to the world's largest desert is unique—even the leading-order balances of the control and perturbation MSE budgets will undoubtedly differ across regions. We do not have a compelling explanation

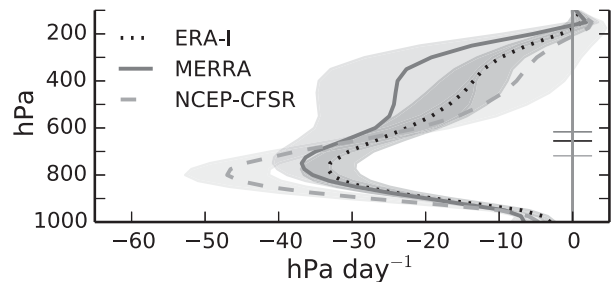


FIG. 12. Sahel region-mean JAS profile of vertical velocity in three reanalysis products. Shaded range denotes plus and minus one standard deviation. Horizontal lines on the vertical axis denote the vertical centroid over the 100–1000-hPa range of the corresponding dataset.

for the errant relationship between cloud radiative properties and precipitation in the Sahel in AM2.1, and thus no a priori reason to expect it to occur in other regions either. The downstream effect on the hydrological cycle will also be modified by the surface energy and water budget—in less water-limited regions, excess shortwave radiation impinging on the surface with cloud loss may counteract the initial precipitation loss, if it drives increased evapotranspiration.

c. On the emergent observational constraint approach

Supposing that a physical link does exist between the precipitation response and the climatological ascent profile structure, to be revealed by, for example, more refined statistical methods, it is worth assessing the extent to which the real-world ascent profile structure can be ascertained. We have analyzed the Sahel JAS region-mean vertical velocity in three reanalysis products: ERA-Interim (Dee et al. 2011) averaged over 1979–2013, NASA-MERRA (Rienecker et al. 2011) averaged over 1979–2011, and NCEP-CFSR (Saha et al. 2010) averaged over 1979–2013. The resulting profiles are shown in Fig. 12. All three exhibit ascent throughout the troposphere that peaks near ~800 hPa. But otherwise they vary markedly from top-heavy (MERRA) to bottom-heavy (NCEP-CFSR), with their average (not shown) largely resembling ERA-Interim.

This large spread among the three reanalysis products analyzed limits the stringency of the resulting observational constraint that could be inferred. Though they assimilate observational data from multiple sources, reanalyses also ultimately rely on a convective parameterization in their underlying dynamical model. The sensitivity of AM2.1 to the convective parameterization (H17) suggests that the reanalyses therefore may not provide a truly reliable constraint. Zhang et al. (2008) find large discrepancies among three reanalyses in their representation of shallow meridional circulations in

multiple tropical regions, including West Africa, and speculate that differences in the convective parameterization, in particular their sensitivity to dry air intrusions, are a key factor. It is interesting to note that MERRA, which generates the most top-heavy profile, uses, like AM2.1, the relaxed Arakawa–Schubert convective parameterization; ERA-Interim and NCEP-CFSR use the simplified Arakawa–Schubert and Tiedtke (1989) schemes, respectively.

With these caveats in mind, we note that NCEP-CFSR's profile is roughly as bottom-heavy as the models' most bottom-heavy profiles (c48-HiRAM and BCC-CSM1.1; cf. Figs. 6a and 7a, respectively), but there are several models (AM2.1, AM2.5, CNRM-CM5, and MIROC5) that are more top-heavy than the most top-heavy reanalysis product (MERRA). Moreover, these models are among those in which SST warming causes the strongest anomalous descent in the free troposphere (Figs. 6d and 7b) and precipitation decrease (Tables 3 and 4). This is broadly consistent with the argument that deeper climatological convection tends to generate greater drying responses to warming.

One plausible factor contributing to the statistical weakness of the relationships between anomalous precipitation and other fields across the CMIP5 models is internally generated variability. The use of large ensembles and the “dynamical adjustment” technique that reduces the influence of internal variability (Deser et al. 2016, and references therein) could therefore be a useful tool.

d. Region definition

In some models (e.g., BCC-CSM1.1 and IPSL-CM5B-LR), the sharp meridional gradients in precipitation and other hydrological fields that in the real world reside in (and essentially define) the Sahel sit instead along the southern border of the region as we have defined it. As such, the climate averaged over our Sahel “box” is essentially all desert, making the physical arguments we have proposed less relevant. It could thus prove fruitful to use a data-driven region definition in future model comparison efforts, such as defining the Sahel as African land points within $\pm 10^\circ$ latitude of the northernmost 3 mm day⁻¹ precipitation isoline on the continent.

8. Summary

We have investigated the hydrological responses in the Sahel region of Africa to a uniform 2-K SST warming in seven NOAA Geophysical Fluid Dynamics Laboratory (GFDL) atmospheric general circulation model (AGCM) variants and to a 4-K SST warming in 10 AGCMs from phase 5 of the Coupled Model Intercomparison

Project (CMIP5). Four of seven GFDL AGCMs and 10 of 10 CMIP5 AGCMs respond to uniform SST warming with reduced wet-season total and convective precipitation in the Sahel. Sixteen of the 17 AGCMs respond with reduced precipitation minus evapotranspiration and boundary layer relative humidity. All 17 AGCMs respond with reduced large-scale precipitation and, over some appreciable fraction of the free troposphere, increased meridional MSE gradient and divergence of MSE by horizontal advection and anomalous subsidence. The three outlier GFDL models all use the Bretherton et al. (2004) (i.e., UW) convective parameterization, which is apparently invigorated with warming, yielding moderately increased total precipitation, convective precipitation, and evapotranspiration. Otherwise, these consistent qualitative features bolster the credibility of the general arguments set forth in Hill et al. (2017), namely that the increased meridional MSE gradient that arises with mean SST warming acts to increase the horizontal advection of dry, low-MSE air from the Sahara into the Sahel, thereby suppressing Sahelian moist convection.

Of the 14 models in which Sahel region-mean precipitation decreases with warming, only in AM2.1 does the net column energetic forcing (equivalent to the net top-of-atmosphere radiative flux for a land region) not reduce appreciably with warming. Given some magnitude of anomalous low-MSE Saharan air meridional advection, this reduction in the other models enables column energy balance to be restored with less anomalous subsidence. As such, this weak forcing response in AM2.1, which results from canceling clear-sky and cloudy-sky anomalies, helps explain the severity of the drying in AM2.1 relative to other models.

The speculation by Hill et al. (2017)—namely, that the depth of the climatological convection in the Sahel significantly contributes to how much the column-integrated MSE difference between the Sahel and the Sahara is enhanced with SST warming—is borne out qualitatively for the GFDL models and a subset of the CMIP5 models. As such, it is of interest that the top-heavy ascent profiles of AM2.1 and some of the other drying-most models are well removed from the estimates from three reanalysis products. Nevertheless, the quantitative relationship between anomalous subsidence and reduced precipitation in the Sahel, which is a necessary intermediate step in the link between climatological ascent and the precipitation response to warming, exhibits sufficient ambiguity across the GFDL and CMIP5 models that a formal emergent observational constraint based on this physical mechanism remains elusive.

In terms of interannual variability, observed TOA radiative fluxes from CERES-EBAF and precipitation

observations from GPCP indicate that AM2.1 exhibits an excessive feedback on precipitation variations through the accompanying cloud radiative variations. This mechanism also acts in AM2.1's equilibrium response to uniform SST warming. All else being equal, this casts doubt on the physical plausibility of the strong future drying projections in the Sahel by coupled models using AM2.1.

Acknowledgments. We thank Fanrong Zeng and Larry Horowitz of GFDL for performing the extended AMIP simulations in AM2.1 and AM3, respectively; Isaac Held and Leo Donner for helpful discussions; Bill Boos, Nadir Jeevanjee, Kirsten Findell, and three anonymous reviewers for their insightful reviews of earlier drafts; the “ana4mips” project for providing all reanalysis data used; and Spencer Clark for his work on the “aosp” data analysis package (Hill and Clark 2017) used for a majority of the calculations. S.A.H. was supported first by a Department of Defense National Defense Science and Engineering Graduate Fellowship and subsequently by a National Science Foundation Atmospheric and Geospace Sciences Postdoctoral Research Fellowship (Award 1624740).

REFERENCES

- Anderson, J. L., 2004: The new GFDL global atmosphere and land model AM2-LM2: Evaluation with prescribed SST simulations. *J. Climate*, **17**, 4641–4673, doi: [10.1175/JCLI-3223.1](https://doi.org/10.1175/JCLI-3223.1).
- Arakawa, A., and W. H. Schubert, 1974: Interaction of a cumulus cloud ensemble with the large-scale environment, Part I. *J. Atmos. Sci.*, **31**, 674–701, [https://doi.org/10.1175/1520-0469\(1974\)031<0674:IOACCE>2.0.CO;2](https://doi.org/10.1175/1520-0469(1974)031<0674:IOACCE>2.0.CO;2).
- Biasutti, M., 2013: Forced Sahel rainfall trends in the CMIP5 archive. *J. Geophys. Res. Atmos.*, **118**, 1613–1623, <https://doi.org/10.1002/jgrd.50206>.
- , and A. Giannini, 2006: Robust Sahel drying in response to late 20th century forcings. *Geophys. Res. Lett.*, **33**, L11706, <https://doi.org/10.1029/2006GL026067>.
- Bony, S., G. Bellon, D. Kloke, S. Sherwood, S. Fermepin, and S. Denvil, 2013: Robust direct effect of carbon dioxide on tropical circulation and regional precipitation. *Nat. Geosci.*, **6**, 447–451, <https://doi.org/10.1038/ngeo1799>.
- Bretherton, C. S., J. R. McCaa, and H. Grenier, 2004: A new parameterization for shallow cumulus convection and its application to marine subtropical cloud-topped boundary layers. Part I: Description and 1D results. *Mon. Wea. Rev.*, **132**, 864–882, [https://doi.org/10.1175/1520-0493\(2004\)132<0864:ANPFSF>2.0.CO;2](https://doi.org/10.1175/1520-0493(2004)132<0864:ANPFSF>2.0.CO;2).
- , P. N. Blossey, and M. E. Peters, 2006: Interpretation of simple and cloud-resolving simulations of moist convection–radiation interaction with a mock-Walker circulation. *Theor. Comput. Fluid Dyn.*, **20**, 421–442, <https://doi.org/10.1007/s00162-006-0029-7>.
- Byrne, M. P., and P. A. O’Gorman, 2015: The response of precipitation minus evapotranspiration to climate warming: Why the “wet-get-wetter, dry-get-drier” scaling does not hold over land. *J. Climate*, **28**, 8078–8092, <https://doi.org/10.1175/JCLI-D-15-0369.1>.
- Chadwick, R., H. Douville, and C. B. Skinner, 2017: Timeslice experiments for understanding regional climate projections: Applications to the tropical hydrological cycle and European winter circulation. *Climate Dyn.*, **49**, 3011–3029, <https://doi.org/10.1007/s00382-016-3488-6>.
- Chen, C.-A., J.-Y. Yu, and C. Chou, 2016: Impacts of vertical structure of convection in global warming: The role of shallow convection. *J. Climate*, **29**, 4665–4684, <https://doi.org/10.1175/JCLI-D-15-0563.1>.
- Chou, C., and J. D. Neelin, 2004: Mechanisms of global warming impacts on regional tropical precipitation. *J. Climate*, **17**, 2688–2701, [https://doi.org/10.1175/1520-0442\(2004\)017<2688:MOGWIO>2.0.CO;2](https://doi.org/10.1175/1520-0442(2004)017<2688:MOGWIO>2.0.CO;2).
- Cook, K. H., 1999: Generation of the African easterly jet and its role in determining West African precipitation. *J. Climate*, **12**, 1165–1184, [https://doi.org/10.1175/1520-0442\(1999\)012<1165:GOTAEJ>2.0.CO;2](https://doi.org/10.1175/1520-0442(1999)012<1165:GOTAEJ>2.0.CO;2).
- Dee, D. P., and Coauthors, 2011: The ERA-Interim reanalysis: Configuration and performance of the data assimilation system. *Quart. J. Roy. Meteor. Soc.*, **137**, 553–597, <https://doi.org/10.1002/qj.828>.
- Delworth, T. L., and Coauthors, 2012: Simulated climate and climate change in the GFDL CM2.5 high-resolution coupled climate model. *J. Climate*, **25**, 2755–2781, <https://doi.org/10.1175/JCLI-D-11-00316.1>.
- Derbyshire, S. H., I. Beau, P. Bechtold, J.-Y. Grandpeix, J.-M. Piriou, J.-L. Redelsperger, and P. M. M. Soares, 2004: Sensitivity of moist convection to environmental humidity. *Quart. J. Roy. Meteor. Soc.*, **130**, 3055–3079, <https://doi.org/10.1256/qj.03.130>.
- Deser, C., L. Terray, and A. S. Phillips, 2016: Forced and internal components of winter air temperature trends over North America during the past 50 years: Mechanisms and implications. *J. Climate*, **29**, 2237–2258, <https://doi.org/10.1175/JCLI-D-15-0304.1>.
- Dong, B., and R. Sutton, 2015: Dominant role of greenhouse-gas forcing in the recovery of Sahel rainfall. *Nat. Climate Change*, **5**, 757–760, <https://doi.org/10.1038/nclimate2664>.
- Donner, L. J., 1993: A cumulus parameterization including mass fluxes, vertical momentum dynamics, and mesoscale effects. *J. Atmos. Sci.*, **50**, 889–906, [https://doi.org/10.1175/1520-0469\(1993\)050<0889:ACPIMF>2.0.CO;2](https://doi.org/10.1175/1520-0469(1993)050<0889:ACPIMF>2.0.CO;2).
- , C. J. Seman, R. S. Hemler, and S. Fan, 2001: A cumulus parameterization including mass fluxes, convective vertical velocities, and mesoscale effects: Thermodynamic and hydrological aspects in a general circulation model. *J. Climate*, **14**, 3444–3463, [https://doi.org/10.1175/1520-0442\(2001\)014<3444:ACPIMF>2.0.CO;2](https://doi.org/10.1175/1520-0442(2001)014<3444:ACPIMF>2.0.CO;2).
- , and Coauthors, 2011: The dynamical core, physical parameterizations, and basic simulation characteristics of the atmospheric component AM3 of the GFDL global coupled model CM3. *J. Climate*, **24**, 3484–3519, <https://doi.org/10.1175/2011JCLI3955.1>.
- Emanuel, K. A., J. D. Neelin, and C. S. Bretherton, 1994: On large-scale circulations in convecting atmospheres. *Quart. J. Roy. Meteor. Soc.*, **120**, 1111–1143, <https://doi.org/10.1002/qj.49712051902>.
- Evan, A. T., C. Flamant, C. Lavaysse, C. Kocha, and A. Saci, 2015: Water vapor–forced greenhouse warming over the Sahara Desert and the recent recovery from the Sahelian drought. *J. Climate*, **28**, 108–123, <https://doi.org/10.1175/JCLI-D-14-00039.1>.
- Flannaghan, T. J., S. Fueglistaler, I. M. Held, S. Po-Chedley, B. Wyman, and M. Zhao, 2014: Tropical temperature trends in atmospheric general circulation model simulations and the

- impact of uncertainties in observed SSTs. *J. Geophys. Res. Atmos.*, **119**, 13 327–13 337, <https://doi.org/10.1002/2014JD022365>.
- Gaetani, M., C. Flamant, S. Bastin, S. Janicot, C. Lavaysse, F. Hourdin, P. Braconnot, and S. Bony, 2017: West African monsoon dynamics and precipitation: The competition between global SST warming and CO₂ increase in CMIP5 idealized simulations. *Climate Dyn.*, **48**, 1353–1373, <https://doi.org/10.1007/s00382-016-3146-z>.
- Harris, I., P. Jones, T. Osborn, and D. Lister, 2014: Updated high-resolution grids of monthly climatic observations—The CRU TS3.10 dataset. *Int. J. Climatol.*, **34**, 623–642, <https://doi.org/10.1002/joc.3711>.
- He, J., and B. J. Soden, 2017: A re-examination of the projected subtropical precipitation decline. *Nat. Climate Change*, **7**, 53–57, <https://doi.org/10.1038/nclimate3157>.
- Held, I. M., and B. J. Soden, 2006: Robust responses of the hydrological cycle to global warming. *J. Climate*, **19**, 5686–5699, <https://doi.org/10.1175/JCLI3990.1>.
- , T. L. Delworth, J. Lu, K. L. Findell, and T. R. Knutson, 2005: Simulation of Sahel drought in the 20th and 21st centuries. *Proc. Natl. Acad. Sci. USA*, **102**, 17 891–17 896, <https://doi.org/10.1073/pnas.0509057102>.
- Hill, S. A., 2016: Energetic and hydrological responses of Hadley circulations and the African Sahel to sea surface temperature perturbations. Ph.D. thesis, Princeton University, 186 pp.
- , and S. K. Clark, 2017: Aospv: V0.2. <https://doi.org/10.5281/zenodo.996951>.
- , Y. Ming, I. M. Held, and M. Zhao, 2017: A moist static energy budget–based analysis of the Sahel rainfall response to uniform oceanic warming. *J. Climate*, **30**, 5637–5660, <https://doi.org/10.1175/JCLI-D-16-0785.1>.
- Hurrell, J. W., J. J. Hack, D. Shea, J. M. Caron, and J. Rosinski, 2008: A new sea surface temperature and sea ice boundary dataset for the Community Atmosphere Model. *J. Climate*, **21**, 5145–5153, <https://doi.org/10.1175/2008JCLI2292.1>.
- Inoue, K., and L. E. Back, 2015: Gross moist stability assessment during TOGA COARE: Various interpretations of gross moist stability. *J. Atmos. Sci.*, **72**, 4148–4166, <https://doi.org/10.1175/JAS-D-15-0092.1>.
- Kato, S., and Coauthors, 2018: Surface irradiances of edition 4.0 Clouds and the Earth’s Radiant Energy System (CERES) Energy Balanced and Filled (EBAF) data product. *J. Climate*, **31**, 4501–4527, <https://doi.org/10.1175/JCLI-D-17-0523.1>.
- Klein, S. A., and A. Hall, 2015: Emergent constraints for cloud feedbacks. *Curr. Clim. Change Rep.*, **1**, 276–287, <https://doi.org/10.1007/s40641-015-0027-1>.
- Lintner, B. R., P. Gentine, K. L. Findell, and G. D. Salvucci, 2015: The Budyko and complementary relationships in an idealized model of large-scale land–atmosphere coupling. *Hydrol. Earth Syst. Sci.*, **19**, 2119–2131, <https://doi.org/10.5194/hess-19-2119-2015>.
- Loeb, N. G., and Coauthors, 2018: Clouds and the Earth’s Radiant Energy System (CERES) Energy Balanced and Filled (EBAF) top-of-atmosphere (TOA) edition-4.0 data product. *J. Climate*, **31**, 895–918, <https://doi.org/10.1175/JCLI-D-17-0208.1>.
- Lu, J., and T. L. Delworth, 2005: Oceanic forcing of the late 20th century Sahel drought. *Geophys. Res. Lett.*, **32**, L22706, <https://doi.org/10.1029/2005GL023316>.
- Milly, P. C. D., and A. B. Shmakin, 2002: Global modeling of land water and energy balances. Part I: The Land Dynamics (LaD) Model. *J. Hydrometeorol.*, **3**, 283–299, [https://doi.org/10.1175/1525-7541\(2002\)003<0283:GMOLWA>2.0.CO;2](https://doi.org/10.1175/1525-7541(2002)003<0283:GMOLWA>2.0.CO;2).
- , and K. A. Dunne, 2016: Potential evapotranspiration and continental drying. *Nat. Climate Change*, **6**, 946–949, <https://doi.org/10.1038/nclimate3046>.
- , and Coauthors, 2014: An enhanced model of land water and energy for global hydrologic and Earth-system studies. *J. Hydrometeorol.*, **15**, 1739–1761, <https://doi.org/10.1175/JHM-D-13-0162.1>.
- Ming, Y., V. Ramaswamy, L. J. Donner, and V. T. J. Phillips, 2006: A new parameterization of cloud droplet activation applicable to general circulation models. *J. Atmos. Sci.*, **63**, 1348–1356, <https://doi.org/10.1175/JAS3686.1>.
- , —, —, —, S. A. Klein, P. A. Ginoux, and L. W. Horowitz, 2007: Modeling the interactions between aerosols and liquid water clouds with a self-consistent cloud scheme in a general circulation model. *J. Atmos. Sci.*, **64**, 1189–1209, <https://doi.org/10.1175/JAS3874.1>.
- Mitchell, J. F. B., C. A. Wilson, and W. M. Cunnington, 1987: On CO₂ climate sensitivity and model dependence of results. *Quart. J. Roy. Meteor. Soc.*, **113**, 293–322, <https://doi.org/10.1002/qj.49711347517>.
- Moorathi, S., and M. J. Suarez, 1992: Relaxed Arakawa–Schubert: A parameterization of moist convection for general circulation models. *Mon. Wea. Rev.*, **120**, 978–1002, [https://doi.org/10.1175/1520-0493\(1992\)120<0978:RASAP0>2.0.CO;2](https://doi.org/10.1175/1520-0493(1992)120<0978:RASAP0>2.0.CO;2).
- Neelin, J. D., and I. M. Held, 1987: Modeling tropical convergence based on the moist static energy budget. *Mon. Wea. Rev.*, **115**, 3–12, [https://doi.org/10.1175/1520-0493\(1987\)115<0003:MTCBOT>2.0.CO;2](https://doi.org/10.1175/1520-0493(1987)115<0003:MTCBOT>2.0.CO;2).
- Nicholson, S. E., 2013: The West African Sahel: A review of recent studies on the rainfall regime and its interannual variability. *ISRN Meteorol.*, 2013, e453521, <https://doi.org/10.1155/2013/453521>.
- , 2018: The ITCZ and the seasonal cycle over equatorial Africa. *Bull. Amer. Meteor. Soc.*, **99**, 337–348, <https://doi.org/10.1175/BAMS-D-16-0287.1>.
- Park, J.-Y., J. Bader, and D. Matei, 2015: Northern-hemispheric differential warming is the key to understanding the discrepancies in the projected Sahel rainfall. *Nat. Commun.*, **6**, 5985, <https://doi.org/10.1038/ncomms6985>.
- Pomposi, C., A. Giannini, Y. Kushnir, and D. E. Lee, 2016: Understanding Pacific Ocean influence on interannual precipitation variability in the Sahel. *Geophys. Res. Lett.*, **43**, 9234–9242, <https://doi.org/10.1002/2016GL069980>.
- Rayner, N. A., D. E. Parker, E. B. Horton, C. K. Folland, L. V. Alexander, D. P. Rowell, E. C. Kent, and A. Kaplan, 2003: Global analyses of sea surface temperature, sea ice, and night marine air temperature since the late nineteenth century. *J. Geophys. Res.*, **108**, 4407, <https://doi.org/10.1029/2002JD002670>.
- Reynolds, R. W., N. A. Rayner, T. M. Smith, D. C. Stokes, and W. Wang, 2002: An improved in situ and satellite SST analysis for climate. *J. Climate*, **15**, 1609–1625, [https://doi.org/10.1175/1520-0442\(2002\)015<1609:AISAS>2.0.CO;2](https://doi.org/10.1175/1520-0442(2002)015<1609:AISAS>2.0.CO;2).
- Rienecker, M. M., and Coauthors, 2011: MERRA: NASA’s Modern-Era Retrospective Analysis for Research and Applications. *J. Climate*, **24**, 3624–3648, <https://doi.org/10.1175/JCLI-D-11-00015.1>.
- Roderick, M. L., F. Sun, W. H. Lim, and G. D. Farquhar, 2014: A general framework for understanding the response of the water cycle to global warming over land and ocean. *Hydrol. Earth Syst. Sci.*, **18**, 1575–1589, <https://doi.org/10.5194/hess-18-1575-2014>.
- Rodríguez-Fonseca, B., and Coauthors, 2015: Variability and predictability of West African droughts: A review on the role of sea surface temperature anomalies. *J. Climate*, **28**, 4034–4060, <https://doi.org/10.1175/JCLI-D-14-00130.1>.

- Saha, S., and Coauthors, 2010: The NCEP Climate Forecast System Reanalysis. *Bull. Amer. Meteor. Soc.*, **91**, 1015–1057, <https://doi.org/10.1175/2010BAMS3001.1>.
- Scheff, J., R. Seager, H. Liu, and S. Coats, 2017: Are glacials dry? Consequences for paleoclimatology and for greenhouse warming. *J. Climate*, **30**, 6593–6609, <https://doi.org/10.1175/JCLI-D-16-0854.1>.
- Seager, R., and N. Henderson, 2013: Diagnostic computation of moisture budgets in the ERA-Interim reanalysis with reference to analysis of CMIP-archived atmospheric model data. *J. Climate*, **26**, 7876–7901, <https://doi.org/10.1175/JCLI-D-13-00018.1>.
- Shekhar, R., and W. R. Boos, 2017: Weakening and shifting of the Saharan shallow meridional circulation during wet years of the West African monsoon. *J. Climate*, **30**, 7399–7422, <https://doi.org/10.1175/JCLI-D-16-0696.1>.
- Singh, M. S., and P. A. O’Gorman, 2012: Upward shift of the atmospheric general circulation under global warming: Theory and simulations. *J. Climate*, **25**, 8259–8276, <https://doi.org/10.1175/JCLI-D-11-00699.1>.
- Sobel, A. H., and G. Bellon, 2009: The effect of imposed drying on parameterized deep convection. *J. Atmos. Sci.*, **66**, 2085–2096, <https://doi.org/10.1175/2008JAS2926.1>.
- Taylor, K. E., R. J. Stouffer, and G. A. Meehl, 2012: An overview of CMIP5 and the experiment design. *Bull. Amer. Meteor. Soc.*, **93**, 485–498, <https://doi.org/10.1175/BAMS-D-11-00094.1>.
- Tiedtke, M., 1989: A comprehensive mass flux scheme for cumulus parameterization in large-scale models. *Mon. Wea. Rev.*, **117**, 1779–1800, [https://doi.org/10.1175/1520-0493\(1989\)117<1779:ACMFSF>2.0.CO;2](https://doi.org/10.1175/1520-0493(1989)117<1779:ACMFSF>2.0.CO;2).
- Tierney, J. E., F. S. R. Pausata, and P. B. deMenocal, 2017: Rainfall regimes of the Green Sahara. *Sci. Adv.*, **3**, e1601503, <https://doi.org/10.1126/sciadv.1601503>.
- Voigt, A., and Coauthors, 2016: The Tropical Rain Belts with an Annual Cycle and a Continent Model Intercomparison Project: TRACMIP. *J. Adv. Model. Earth Syst.*, **8**, 1868–1891, <https://doi.org/10.1002/2016MS000748>.
- Wang, S., and A. H. Sobel, 2012: Impact of imposed drying on deep convection in a cloud-resolving model. *J. Geophys. Res.*, **117**, D02112, <https://doi.org/10.1029/2011JD016847>.
- Zhai, J., and W. R. Boos, 2017: The drying tendency of shallow meridional circulations in monsoons. *Quart. J. Roy. Meteor. Soc.*, **143**, 2655–2664, <https://doi.org/10.1002/qj.3091>.
- Zhang, C., D. S. Nolan, C. D. Thorncroft, and H. Nguyen, 2008: Shallow meridional circulations in the tropical atmosphere. *J. Climate*, **21**, 3453–3470, <https://doi.org/10.1175/2007JCLI1870.1>.
- Zhao, M., 2014: An investigation of the connections among convection, clouds, and climate sensitivity in a global climate model. *J. Climate*, **27**, 1845–1862, <https://doi.org/10.1175/JCLI-D-13-00145.1>.
- , I. M. Held, S.-J. Lin, and G. A. Vecchi, 2009: Simulations of global hurricane climatology, interannual variability, and response to global warming using a 50-km resolution GCM. *J. Climate*, **22**, 6653–6678, <https://doi.org/10.1175/2009JCLI3049.1>.
- Zhou, L., M. Zhang, Q. Bao, and Y. Liu, 2015: On the incident solar radiation in CMIP5 models. *Geophys. Res. Lett.*, **42**, 1930–1935, <https://doi.org/10.1002/2015GL063239>.